

Geometric Shaping for Distortion-Limited Intensity Modulation/Direct Detection Data Center Links

Ethan M. Liang , Graduate Student Member, IEEE, and Joseph M. Kahn , Fellow, IEEE

Abstract—Intra-data center links are subject to transmission impairments that pose challenges for efficient scaling of per-wavelength data rates beyond 100 Gb/s. Limited electrical and optical component bandwidths, limited data converter resolution, and direct detection induce significant signal-dependent distortion, degrading receiver sensitivity (RS) and chromatic dispersion tolerance. In this paper, we present a geometric shaping (GS) scheme that optimizes transmitted intensity levels based on symbol-error statistics observed at the receiver. The proposed GS scheme adjusts these levels to achieve substantially equal symbol-error probabilities at all decision thresholds. The scheme enables the levels most affected by signal-dependent distortion to be detected with the same reliability as other levels, thereby increasing the effectiveness of linear or nonlinear equalization techniques. This can be exploited to improve RS and extend transmission distance for a fixed equalization scheme or, alternatively, to reduce the complexity of signal processing needed to achieve a target RS or transmission distance. For example, in 200 Gb/s PAM links, GS and 21-tap linear equalization achieves RS and reach similar to uniform level spacing and Volterra nonlinear equalization with 21 linear and 3 second-order taps.

Index Terms—Geometric shaping, direct detection, optical communications.

I. INTRODUCTION

ARISE in global Internet traffic, primarily from video and machine-learning applications, has caused a massive increase in intra-data center (DC) bandwidth requirements [1]. To meet these demands, many data center operators have adopted high per-wavelength data rates and coarse wavelength-division multiplexing (CWDM) [1], [2] or other forms of WDM. Intra-DC optical links are often subdivided into two categories [3]. The shortest-reach optical links have lengths up to a few hundred meters and traditionally have used multi-mode fiber (MMF). Intra-DC links beyond this length use single-mode fiber (SMF) to avoid modal dispersion [4]. Using multilevel pulse-amplitude modulation (PAM) and direct detection (DD) at data rates up to 100 Gb/s per wavelength, they typically achieve maximum link lengths ranging from 2 to 20 km. These intra-DC links are the focus of this paper.

Manuscript received 19 October 2023; revised 10 November 2023; accepted 15 November 2023. Date of publication 22 November 2023; date of current version 12 December 2023. This work was supported in part by Maxim Integrated (Analog Devices, Inc.), Inphi Corporation (Marvell) and in part by the National Science Foundation under Grant DGE-1656518. (Corresponding author: Ethan M. Liang.)

The authors are with the E. L. Ginzton Laboratory, Department of Electrical Engineering, Stanford University, Stanford, CA 94305 USA (e-mail: emliang@stanford.edu; jmk@ee.stanford.edu).

Digital Object Identifier 10.1109/JPHOT.2023.3335398

Efficiently scaling intra-DC links beyond 100 Gb/s per wavelength will require the mitigation of two key impairments. First, intra-DC transceivers use small-form-factor components that often have low bandwidth and substantial nonlinearity, which combine to cause considerable distortion [3]. Second, the combination of chromatic dispersion (CD) with DD results in nonlinear distortion, and the effects of CD are exacerbated by CWDM, which employs wavelengths away from the dispersion zero. The above-mentioned forms of distortion cause intersymbol interference (ISI). Since the amount of ISI typically differs from one signal level to another, we refer to these forms of distortion collectively as *signal-dependent distortion*.

Geometric shaping (GS) provides a method to reduce the impact of signal-dependent distortion in DD optical links. GS is often defined as the optimization of the locations of constellation points (which are intensity levels in DD systems) according to some specified criterion [5]. In this paper, we focus on minimizing signal-dependent distortion arising from transmitter bandwidth limitations and CD in unamplified DD links. Various GS schemes using conventional optimization techniques [6], [7], [8], [9], [10], [11], [12], [13] or machine learning [14], [15], [16] have been previously proposed for intensity modulation (IM)/DD optical links. While GS schemes using autoencoders or other machine learning techniques have been used to improve the performance of various optical links [14], [15], [16], [17], [18], [19], the strict cost and complexity limits on intra-DC links lead us to focus primarily on non-machine learning-based GS schemes. Among schemes using conventional optimization techniques, all previously proposed GS schemes for IM/DD links either parameterize the signal constellation by up to several variables or assume the noise distribution at the receiver follows a Gaussian distribution. These assumptions limit the effectiveness of these previously proposed GS schemes in IM/DD links in which nonlinear signal-dependent distortion is a significant factor.

In this paper, we use GS to reduce the impact of signal-dependent distortion on receiver sensitivity (RS) in unamplified DD optical links. Our proposed GS algorithm distinguishes itself from previously proposed GS schemes for DD-based optical interconnects by achieving the optimization objective without parameterizing the signal constellation nor assuming the dominant noise source follows a Gaussian distribution. The proposed GS scheme reduces the impact of signal-dependent distortion by increasing the distance between intensity levels most affected by distortion. The resulting optimized signal constellation causes each level to be detected with the same fidelity as any other level,

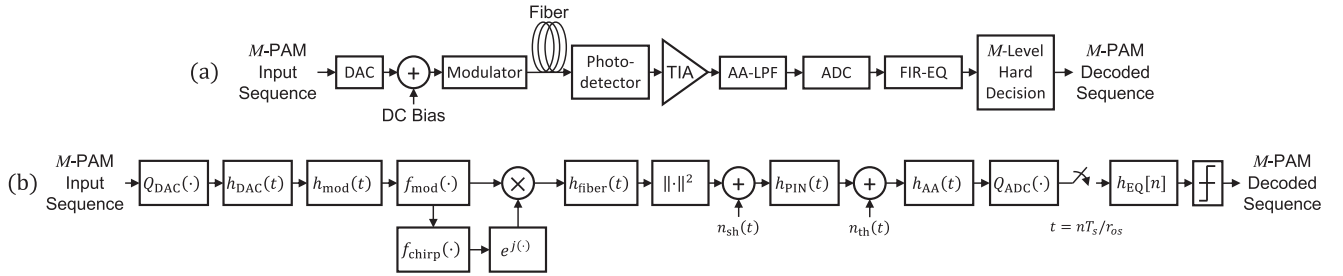


Fig. 1. (a) Block diagram of an IM/DD optical link without optical amplification. (b) The corresponding equivalent baseband model.

thereby improving equalizer performance, RS, and transmission reach. The proposed scheme can alternatively be used to reduce the complexity of the signal processing required to achieve a target RS or transmission reach. We also study data converter resolution requirements and show that the proposed GS scheme can reduce the impact of finite data converter resolution. While we use GS to reduce the impact of distortion arising from modulator nonlinearities, CD, and data converters, the proposed GS scheme can be straightforwardly used to compensate for other forms of signal-dependent distortion. Although current intra-DC interconnects typically use *p-i-n* photodetectors that produce signal-independent noise, the proposed GS scheme can also mitigate signal-dependent noise, as in DD receivers using APDs or SOAs [7].

The remainder of the paper is organized as follows. Section II introduces the system model, emphasizing the modeling of modulators, which are important sources of signal-dependent distortion in IM/DD links. Section III presents the proposed GS scheme and the performance metrics that are used to evaluate the efficacy of the proposed scheme. Section IV quantifies the performance benefit of GS in combating bandwidth limitations and chromatic dispersion in systems using linear equalization and Volterra nonlinear equalization. Section V studies GS for 200 Gb/s-per-wavelength CWDM intra-DC links, including data converter resolution, drive signal optimization, and implementation complexity. Section VI concludes the paper.

II. SYSTEM MODEL

In this section, we describe our model for IM/DD optical links, placing emphasis on modulator modeling. We define the relevant notation and present the system design parameters assumed throughout the paper.

A. Overview

Fig. 1(a) and (b) depict a block diagram and equivalent baseband model for an IM/DD optical link, respectively. We first use the block diagram to describe the set of link components that constitute the IM/DD link model. We then derive the equivalent baseband model from the block diagram using analytical models for each of the constituent components. The equivalent baseband model in Fig. 1(b) is employed in our numerical simulations.

Fig. 1(a) begins with a finite sequence of M -PAM symbols. The digital-to-analog converter (DAC) transforms the

M -PAM sequence into a sequence of voltages that are subsequently input to the modulator. The resulting modulated optical signal is transmitted through the fiber to the receiver, where it is converted to a current by the photodetector. The trans-impedance amplifier (TIA) converts the current into a usable voltage, which is subsequently filtered by the anti-aliasing (AA) low-pass filter (LPF). The filtered voltage signal is sampled by the analog-to-digital converter (ADC) to generate a sampled sequence. A finite impulse response (FIR) equalizer (EQ) processes the sampled sequence to reduce ISI. The resulting sequence is mapped to a decoded M -PAM sequence by the hard-decision device.

The equivalent baseband model in Fig. 1(b) also begins with a finite sequence of M -PAM symbols a_0, a_1, \dots, a_{N-1} of length N . The i th transmitted symbol assumes one of M possible values $a_i \in \{A_0, \dots, A_{M-1}\}$, where A_j denotes the j th symbol in the M -PAM alphabet. The symbol sequence is input to the DAC, which generates an analog electrical drive signal $V(t)$. The target amplitudes of the analog drive signal are designed to achieve a specified set of output powers in the transmitted optical signal after accounting for the modulator nonlinear transfer characteristic $f_{mod}(\cdot)$. The target output powers $\{P_0, P_1, \dots, P_{M-1}\}$ are mapped to the pre-distorted voltage amplitudes $\{V_0, V_1, \dots, V_{M-1}\}$ by the inverse modulator characteristic $f_{mod}^{-1}(\cdot)$. The resulting peak-to-peak voltage is given by $V_{pp} = |V_{M-1} - V_0|$. The extinction ratio r_{ex} is defined as the ratio of the maximum and minimum powers at the modulator output.

The M -PAM input sequence assumes voltage amplitudes from the set $\{V_0, V_1, \dots, V_{M-1}\}$. The voltage sequence is quantized by the function Q_{DAC} , which is parameterized by a full-scale interval $\Delta_{DAC} = [\Delta_{DAC, \min}, \Delta_{DAC, \max}]$, clipping ratio r_{DAC} , and resolution B_{DAC} [20]. We assume Δ_{DAC} is centered with respect to the input sequence minimum and maximum. r_{DAC} is defined as the ratio of $\Delta_{DAC, \max} - \Delta_{DAC, \min}$ to V_{pp} . For each simulation, r_{DAC} is chosen to minimize the empirical mean-squared difference between the unquantized input sequence and the quantized output sequence. The DAC codebook consists of values equally spaced over the interval Δ_{DAC} , and each element of the input sequence is quantized to the nearest value in the codebook. Similar to [21], the bandwidth limitations of the DAC are described by an impulse response $h_{DAC}(t)$, which is the cascade of a zero-order hold filter and a 5th-order Bessel filter. As seen in the baseband model of Fig. 1(b), the overall transmitter

bandwidth limitation results from the convolution of $h_{\text{DAC}}(t)$ and the modulator impulse response $h_{\text{mod}}(t)$.

The nonlinear characteristics of the modulator follow the linear low-pass filtering effects of $h_{\text{mod}}(t)$. The two effects captured in our model are the instantaneous nonlinear transfer characteristic $f_{\text{mod}}(\cdot)$ and modulator chirp $f_{\text{chirp}}(\cdot)$. We defer further discussion of the modulator model to Section II-B.

After modulation, the signal is coupled into an SMF with zero-dispersion wavelength λ_0 and dispersion slope parameter S_0 , yielding a dispersion parameter given by

$$D(\lambda) = \frac{S_0}{4} \left(\lambda - \frac{\lambda_0^4}{\lambda^3} \right), \quad (1)$$

where λ is the wavelength of the optical signal. We model the dispersion on each channel using the dispersion parameter at its center frequency.

After transmission through the SMF, the transmitted optical signal $E(t)$ is detected at the receiver using a PIN photodetector, generating electrical current $I(t)$. Shot noise is added with one-sided power spectral density (PSD)

$$S_{\text{shot}}(f) = 2q(RP_{\text{rec}} + I_d), \quad (2)$$

where q is the electron charge, R is the responsivity of the photodetector, P_{rec} is the received optical power and I_d is the dark current [22]. The current is converted to a usable voltage by the TIA with input-referred noise I_n . I_n is related to the one-sided AWGN PSD of the thermal noise by $N_0 = I_n^2$. Thermal noise is dominant in well-designed unamplified IM/DD links, so we neglect any impact of relative intensity noise (RIN) [23].

The detected voltage is input to an analog 4th-order Butterworth LPF with cutoff frequency $f_{3\text{dB,AA}} = 0.5 \cdot R_s \cdot r_{\text{os}}$, where R_s is the baud rate and r_{os} is an oversampling rate. The filtered electrical signal is input to the ADC with a specified effective number of bits (ENOB) and sampled at a sampling rate of $R_s \cdot r_{\text{os}}$. The effects of bandwidth limitations and nonlinear distortion are partially compensated using an adaptive, fractionally spaced finite impulse response equalizer (FIR-EQ) with $r_{\text{os}} = 5/4$, which is updated using the least mean squares algorithm. We analyze both linear feed-forward equalization (FFE) and second-order Volterra nonlinear equalization (VNLE) in this paper. The memory lengths for the first-order linear kernel and the second-order nonlinear kernel are $n_{\text{taps},1}$ and $n_{\text{taps},2}$, respectively. The real-valued equalizer output sequence of length N is denoted b_0, b_1, \dots, b_{N-1} .

A hard-decision decoder with $M - 1$ inner decision levels $b_{th,1}, b_{th,2}, \dots, b_{th,M-1}$ and two outer decision thresholds $b_{th,0}$ and $b_{th,M}$ maps the equalizer output to a detected M -PAM symbol sequence $\hat{a}_0, \hat{a}_1, \dots, \hat{a}_{N-1}$. The outer decision thresholds are defined as $b_{th,0} = -\infty$ and $b_{th,M} = +\infty$. The i th detected symbol is $\hat{a}_i = A_j$ when $b \in (b_{th,j}, b_{th,j+1})$. A symbol error on the i th transmitted symbol occurs when $a_i \neq \hat{a}_i$. The decoded symbol sequence is mapped to a decoded bit sequence using Gray coding if M is a power of two or the 2-dimensional 6-PAM mapping described in [24] when $M = 6$. The bit-error ratio (BER) is computed on the subset of decoded bits after the adaptive equalizer has converged. Denoted by $\text{BER}_{\text{target}}$, the pre-forward error-correction (pre-FEC) threshold

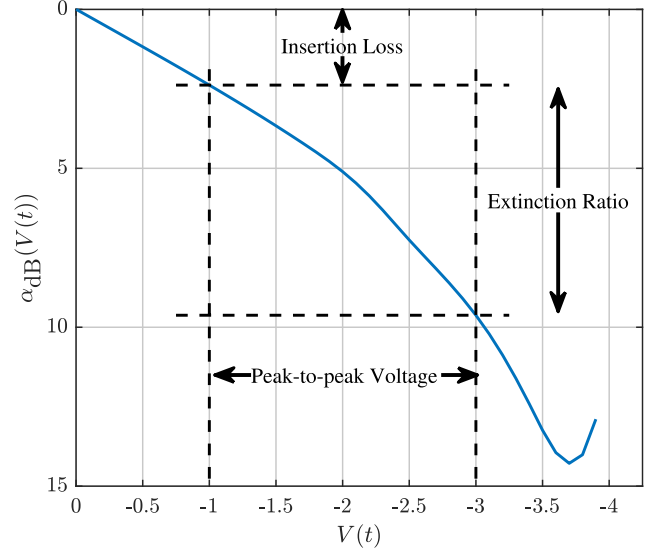


Fig. 2. EAM absorption vs. drive voltage based on [29]. The solid line represents the instantaneous transfer characteristic and the dashed lines denote the region over which the EAM is operated, assuming the modulator is biased at an insertion loss of 2.38 dB and a peak-to-peak voltage of 2 V. The insertion loss, extinction ratio, and peak-to-peak voltage are indicated by the dashed lines.

BER is 1.8×10^{-4} , slightly below the 6.25% overhead KP4-FEC threshold BER of 2.4×10^{-4} [25].

B. Electro-Absorption Modulator

As intra-DC links have shifted from binary to multi-level modulation, these links have shifted toward external modulators [2], [26], [27]. In our model, we assume an electro-absorption modulator (EAM), owing to its advantages for intra-DC links [28]. Compared to directly modulated lasers, EAMs generally have a wider modulation bandwidth, a smaller linewidth enhancement factor, and a larger extinction ratio. Compared to Mach-Zehnder modulators, EAMs are typically smaller, consume less power, and require lower driving voltages.

Various models can capture modulator nonlinearity, including memoryless nonlinear transfer characteristics [30], Volterra series [31], or finite-difference time-domain models [32]. We model the EAM as a Wiener system, which comprises a linear system with memory followed by a memoryless nonlinear system. Following common practice, we model the bandwidth limitations of EAMs using a two-pole LPF with 3-dB cutoff frequency $f_{3\text{dB,mod}}$ [33]. The instantaneous nonlinearity is modeled using a voltage-to-absorption transfer characteristic $\alpha_{\text{dB}}(V(t))$. Fig. 2 depicts the transfer characteristic of the EAM used in our analysis, which is derived from [29] using a cubic spline fit. The insertion loss (IL), extinction ratio, and peak-to-peak voltage are depicted in the figure. Assuming a fixed input laser power, the relationship between the transmitted electrical field amplitude and the drive voltage is given by

$$|E(t)| = f_{\text{mod}}(V(t)) = \sqrt{P_{\text{in}} \cdot 10^{-\alpha_{\text{dB}}(V(t))/10}}. \quad (3)$$

The Kramers-Kronig relations imply that electro-absorption-based intensity modulation necessarily leads to phase modulation of the optical signal. In EAMs, transient chirp is the

TABLE I
SIMULATION PARAMETERS

System Parameters	R_b	212 Gb/s
	M	4, 6, or 8
	BER _{target}	1.8×10^{-4}
Modulator	GS	yes or no
	$f_{3dB,mod}$	40, 50, or 65 GHz
	V_{pp}	1.5, 2, 2.5, or 3 V
	r_{ex}	varies
	IL	varies
	nonlinear model	Wiener system
DAC	α	varies
	$f_{3dB,DAC}$	$f_{3dB,mod}$ or ∞ Hz
SMF	resolution	5, 6, or ∞ b
	λ_0	1310 nm
	S_0	0.092 ps/(nm ² · km)
PIN Photodetector	R	1 A/W
	$f_{3dB,PIN}$	$f_{3dB,mod}$ or ∞ Hz
	I_d	0 or 10 nA
TIA	I_n	30 pA/ $\sqrt{\text{Hz}}$
ADC	ENOB	5, 6, or ∞ b
	r_{os}	5/4
Anti-Aliasing Filter	type	4 th order Butterworth
	$f_{3dB,AA}$	$0.5 \cdot R_s \cdot r_{os}$ Hz
Linear or Nonlinear Equalizer	$n_{taps,1}$	21
	$n_{taps,2}$	varies
Laser	RIN	$-\infty$ dB/Hz

dominant source of phase modulation [34], [35] and is modeled by a transient phase shift

$$\Delta\phi(t) = f_{\text{chirp}}(|E(t)|) = \frac{\alpha}{2} \ln(|E(t)|^2), \quad (4)$$

where α is the linewidth enhancement factor. In general, α is a function of the applied voltage and can be designed to fall within a certain range [32], [36]. In this paper, we study α over a range of [0, 3] and assume α is independent of the applied voltage to reduce the dependency on a specific modulator model. When not explicitly studying the effect of varying α , we often assume $\alpha = 2$ to represent a relatively high, but practically relevant value for the modulator chirp.

C. Simulation Parameters

The simulation parameters used in this study are listed in Table I. A row with exactly one numerical value indicates that the value is used in all simulations presented. Rows with two or more numerical values indicate simulation parameters that vary across different simulations. The parameter values used in a given numerical simulation are provided either in the associated figure caption or legend, except when the values can be inferred. r_{ex} and V_{pp} are one such example, as only one is typically specified to avoid providing redundant information.

III. GEOMETRIC SHAPING

Constellation shaping typically refers to the optimization of a transmitted constellation according to some criterion. Optimization criteria may include metrics such as mutual information, generalized mutual information, or symbol-error probability [37]. In probabilistic shaping (PS), the input probability distribution is optimized while keeping the location of the constellation points fixed, while in GS, the locations of the constellation points are optimized without modifying their distribution.

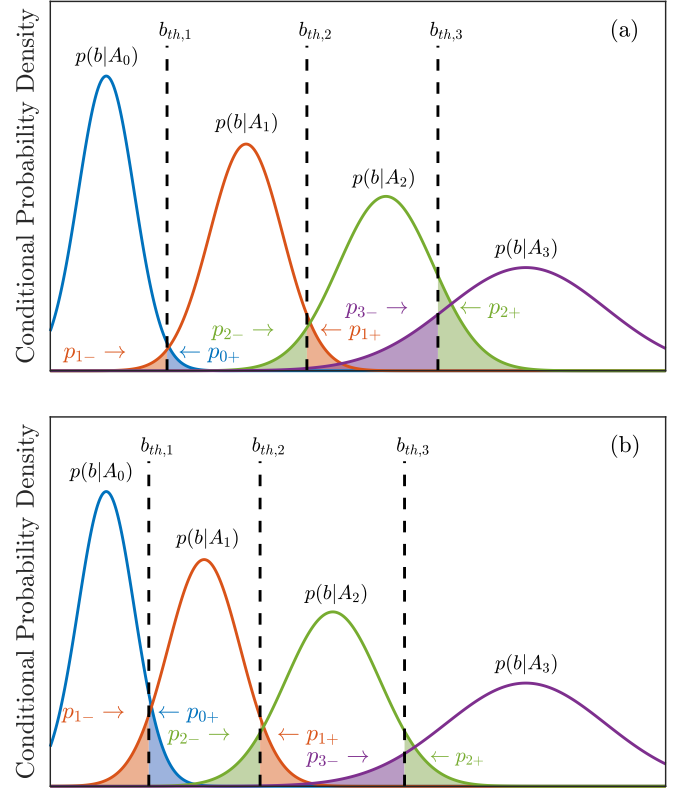


Fig. 3. PDFs of the equalizer output b conditioned on a transmitted symbol A_j , $j \in \{0, 1, 2, 3\}$. $p_{j,+}$ and $p_{j,-}$ denote the probabilities, conditioned on the transmission of symbol A_j , that b is below and above $b_{th,j}$ and $b_{th,j+1}$, respectively. The $b_{th,j}$, $j = 1, 2, 3$ are chosen such that $p_{j-1,+} \approx p_{j,-}$. In (a), the mean values of the conditional PDFs are uniformly spaced. In (b), the means of b conditioned on A_0 and A_3 are unchanged from part (a), while the means of b conditioned on A_1 and A_2 are shifted so that $p_{j,-} \approx p_{j,+}$ for $j = 1, 2$.

In this section, we present our proposed GS scheme and the algorithmic implementation used throughout the paper. We then introduce a set of performance metrics that are used throughout the paper to quantify the benefits of the proposed scheme. Our terminology and notation are specific to IM/DD systems using M -PAM.

A. Proposed Geometric Shaping Scheme

In many IM/DD systems, the detected electrical signal is subject to significant signal-dependent distortion, and optimizing the transmitted intensity levels to account for this distortion may improve overall system performance. Signal-dependent distortion in unamplified IM/DD links can arise from a combination of component bandwidth limitations and nonlinear transfer characteristics and a combination of CD, modulator chirp, and DD. These two sources of signal-dependent distortion are analyzed further in Section IV. In presenting the proposed GS scheme, we first describe the optimization method using generic probability density functions (PDFs), then present a specific algorithm used for optimizing the transmitted intensity levels.

Fig. 3(a) and (b) depict generic conditional PDFs of the equalizer output b given a transmitted symbol A_j , which are denoted $p(b|A_j)$, $j \in \{0, 1, 2, 3\}$. The variances of identically labeled

conditional PDFs are equal in the two subfigures. The variances of the conditional PDFs increase with the index j . In Fig. 3(a), the conditional means of the PDFs are equally spaced. In Fig. 3(b), the means of b conditioned on A_1 and A_2 are shifted from those in Fig. 3(a) so that $p_{j,-} \approx p_{j,+}$ for $j = 1, 2$. Here, $p_{j,+}$ and $p_{j,-}$ denote the probabilities, conditioned on transmission of symbol A_j , that the equalizer output b is above and below the decision thresholds $b_{th,j+1}$ and $b_{th,j}$, respectively. The $b_{th,j}$, $j = 1, 2, 3$ are set so that $p_{j-1,+} \approx p_{j,-}$ and are denoted as *equal-crossover decision thresholds*.

As seen in Fig. 3(a), when equally spaced intensity levels are used, signal-dependent noise and distortion can lead to substantially different symbol-error rates at the various decision thresholds. In the proposed GS scheme, we adjust the transmitted intensity levels, subject to fixed minimum and maximum drive voltage constraints, in order that $p_{j,+} \approx p_{j,-}$, $j = 1, 2, \dots, M - 1$. Using equal-crossover decision thresholds further ensures that $p_{j-1,+} \approx p_{j,-}$, $j = 1, 2, \dots, M - 1$. Conditional PDFs optimized using this scheme are depicted in Fig. 3(b), and result in substantially equal error probabilities at all decision thresholds.

One may contrast equal-crossover decision thresholds with maximum-likelihood (ML) decision thresholds. The ML thresholds $b_{th,j}^{ML}$ would be set such that $p(b_{th,j}^{ML}|A_{j-1}) = p(b_{th,j}^{ML}|A_j)$, $j = 1, 2, M - 1$, i.e., at the crossing points between adjacent conditional PDFs. The ML decision thresholds typically lie close to the respective equal-crossover decision thresholds. Our proposed GS scheme uses equal-crossover decision thresholds instead of ML decision thresholds for two reasons. First, in the proposed GS scheme, equal-crossover decision thresholds are required to achieve the goal of approximately equal error probabilities at all decision thresholds. Second, equal-crossover decision thresholds are found to speed up the convergence of our proposed iterative GS algorithm over ML decision thresholds when distortion is most significant on only a small subset of the transmitted intensity levels.

1) *Geometric Shaping Algorithm*: Algorithm 1 describes an iterative procedure for obtaining a set of drive voltage levels that achieves substantially equal error probabilities at all decision thresholds. The algorithm presumes a fixed drive voltage range defined by minimum and maximum voltages V_0 and V_{M-1} . The algorithm outputs a set of $M - 2$ drive voltages that correspond to the inner transmitted intensity levels.

The GS optimization scheme also takes as input the laser power input to modulator P_{in} , modulation order M , BER_{target} , and constants K , δ , and δ_{min} . K , M , and BER_{target} are used in computing C , which is, in turn, used as a regularization term. $\delta \cdot P_{diff}$ defines the maximum step size, in L1 norm, between $\{P_1^{(i)}, P_2^{(i)}, \dots, P_{M-2}^{(i)}\}$ and $\{P_1^{(i-1)}, P_2^{(i-1)}, \dots, P_{M-2}^{(i-1)}\}$.

Algorithm 1 is inspired by the classic gradient descent algorithm and uses regularized update steps and an adaptive learning rate. Lines 1 through 6 set the initialization values for the algorithm. Lines 7 through 16 constitute the iterative updates to the transmitted intensity levels. The number of symbols N is chosen to be sufficiently large to obtain accurate estimates of $p_{j,-}^{(i)}$ and $p_{j,+}^{(i)}$, which can be updated in an online fashion. The conditional decision error probabilities at the receiver are collected in line 9 and processed into a relative difference metric

Algorithm 1: Geometric Shaping Algorithm.

Input: P_{in} , V_0 , V_{M-1} , δ , δ_{min} , BER_{target} , K , M , N
Output: V_1, V_2, \dots, V_{M-2}

- 1: $i \leftarrow 0$
- 2: $P_0 = P_{in} f_{mod}(V_0)$, $P_{M-1} = P_{in} f_{mod}(V_{M-1})$
- 3: Set $P_0, P_1^{(i)}, P_2^{(i)}, \dots, P_{M-2}^{(i)}, P_{M-1}$ uniformly spaced over the interval $[P_0, P_{M-1}]$
- 4: $P_{diff} = |P_{M-1} - P_0|$
- 5: $V_j^{(i)} \leftarrow f_{mod}^{-1}\left(\frac{P_j^{(i)}}{P_{in}}\right)$, $j = 1, 2, \dots, M - 2$
- 6: $C = \frac{BER_{target}}{2 \cdot (M-1) \cdot K}$
- 7: **while** $\delta \geq \delta_{min}$ **do**
- 8: $i \leftarrow i + 1$
- 9: Transmit N symbols, detect using equal-crossover decision thresholds and note the empirical values for $p_{j,+}^{(i)}$ and $p_{j,-}^{(i)}$, $j = 1, 2, \dots, M - 2$
- 10: $\epsilon_j = \frac{p_{j,-}^{(i)} - p_{j,+}^{(i)}}{p_{j,-}^{(i)} + p_{j,+}^{(i)} + C}$, $j = 1, 2, \dots, M - 2$
- 11: $\Delta_j = \epsilon_j / \left(\sum_{j=1}^{M-2} |\epsilon_j|\right)$, $j = 1, 2, \dots, M - 2$
- 12: $P_j^{(i)} = P_j^{(i-1)} + \delta \cdot \Delta_j \cdot P_{diff}$, $j = 1, 2, \dots, M - 2$
- 13: **if** $i > 1$ & $\left(\sum_{j=1}^{M-2} |P_j^{(i)} - P_j^{(i-2)}|\right) < \delta \cdot P_{diff}$ **then**
- 14: $\delta \leftarrow \delta/2$
- 15: **end if**
- 16: **end while**
- 17: $V_j \leftarrow f_{mod}^{-1}\left(\frac{P_j^{(i)}}{P_{in}}\right)$, $j = 1, \dots, M - 2$

ϵ_j in line 10. ϵ_j is normalized to have unit L1 norm and then used to update the transmitted intensity levels. The algorithmic complexity of computing $P_j^{(i)}$ in each update step is $\mathcal{O}(M)$, which is independent of N .

Line 13 in Algorithm 1 is a condition to infer whether the transmitted intensity levels have converged to the vicinity of some fixed points, and reduces the parameter δ by a factor of 2 when the condition is satisfied. The L1 norm, the decay rate of $\delta \leftarrow \delta/2$, and C are chosen heuristically to speed up convergence to a set of drive voltages achieving substantially equal decision-error probabilities. While other choices for these parameters are possible, Algorithm 1 is found to be capable of identifying intensity levels with substantially equal error probabilities over a wide range of scenarios.

B. Other GS Schemes

Various GS schemes have been proposed and studied over the last several decades for a wide array of optical communication systems [5], [6], [7], [8], [9], [10], [11], [12], [13], [14], [15], [16], [17], [18], [19], [37], [38], [39], [40], [41], [42], [43], [44], [45], [46], [47], [48], [49], [50], [51], [52], [53]. In this subsection, we provide an extensive survey of previously proposed GS schemes and classify them according to their optimization objective and optimization methodology. We then compare the

GS scheme proposed in Algorithm 1 against previously proposed GS schemes for IM/DD links.

1) *Survey of Prior Work*: The optimization objective refers to the metric by which the performance of a particular constellation is evaluated. The previously studied optimization objectives include symbol-error ratio (SER) [9], [10], [11], [47], BER [12], [13], [38], equality of the error probabilities at the decision thresholds [6], [7], [8], average pair-wise hard-decoded error probability [5], [37], [43], [44], [45], mean-square error from a target distribution [5], [37], mutual information or generalized mutual information [37], [40], [41], [42], [48], [51], [52], [53], and Euclidean distance [49].

The optimization methodology refers to the process of designing the locations of the constellation points in order to achieve the desired optimization objective. Some of the optimization methodologies employed in our survey include gradient descent [10], [11], [38], [39], parameterized optimization of up to several variables [12], [13], [40], [41], fixed analytic expressions assuming a Gaussian approximation of the noise [6], [7], [8], [9], [42], iterative pairwise optimization [37], [42], [43], [48], [53], iterative distance-based clustering [5], [37], [44], [45], [46], [47], [48], multi-dimensional modulation [49], [50], [51], and genetic algorithms [52].

Machine learning-based approaches to GS in optical communications can likewise be categorized in terms of their optimization objective and optimization methodology. The structures and loss functions of these schemes specify their optimization objectives. For example, autoencoder-based architectures using categorical cross-entropy and binary cross-entropy as loss functions can be used to optimize for mutual information and generalized mutual information, respectively [19]. Back-propagation, reinforcement learning, and gradient-free methods have been studied previously to design the constellations for various machine learning-based GS schemes [17], [18], [19]. While our analysis focuses primarily on non-machine learning-based approaches to GS, Refs. [17], [18], [19] can provide a comprehensive introduction to machine learning-based methods.

2) *Comparison With Other GS Schemes for IM/DD Links*: Short-reach optical links have traditionally used IM/DD with hard-decision FEC. For these systems, possible natural choices for an optimization objective are BER, SER, or equality of hard-decision error probabilities at all decision thresholds, as each objective is closely related to the RS in systems using hard-decision FEC. Refs. [6], [7], [8], [9], [10], [11], [12], [13] are among the most relevant previously proposed schemes for IM/DD links, each of which uses at least one of the three aforementioned optimization objectives.

While these previous schemes were shown to improve RS of IM/DD links in certain operating regimes, these previously proposed GS schemes either make assumptions about the exact noise distribution at the receiver or parameterize the input constellation by up to several variables. While these assumptions and parameterizations reduce the complexity of the optimization methodologies, they also limit their effectiveness in IM/DD links that are subject to substantial non-Gaussian, signal-dependent distortion. Our proposed GS scheme is distinct from previously

proposed GS schemes for IM/DD links in several ways. In contrast to previous schemes [6], [7], [8], [9], [10], [11], [12], [13], our proposed scheme makes no assumption about the specific noise distribution at the receiver nor parameterizes the signal constellation. In addition, our proposed scheme's optimization methodology is also unique among the surveyed GS schemes. Specifically, the update procedure described in lines 7 through 16 of Algorithm 1 constitutes a novel method that directly uses only the observed symbol-error statistics at the receiver to iteratively optimize all transmitted intensity levels simultaneously. We note the variable δ in Algorithm 1 is somewhat analogous to the trust region described in [39].

The proposed GS scheme also possesses several properties that, taken together, are unique among GS schemes for optical links and are highly desirable in low-complexity IM/DD links. For one, our proposed scheme uses a novel metric of normalized conditional differential error probability Δ_j , which only requires a complexity of $\mathcal{O}(M)$ per iteration. In addition, our algorithm only requires tracking the conditional hard-decision tail error probabilities ($p_{j,+}^{(i)}$ and $p_{j,-}^{(i)}$) at the receiver. By contrast, the surveyed GS schemes that use either iterative pairwise optimization or gradient descent as their optimization methodology and, additionally, do not assume the conditional noise distribution is Gaussian require estimation of the entire conditional posterior distribution at the receiver or have a complexity of at least $\mathcal{O}(M^2)$ per iteration [39], [43].

We end this subsection by noting that machine learning-based approaches to GS for IM/DD systems have been investigated in Refs. [14], [15], [16]. These approaches share some advantageous properties with our proposed scheme. For example, these machine learning-based techniques do not assume a particular analytic distribution for the noise or explicitly parameterize the signal constellation. A more thorough comparison between our proposed GS scheme and this class of techniques should consider the strict cost and complexity constraints of short-reach IM/DD links, and is beyond the scope of this paper.

C. Performance Metrics

The effects of GS and the aforementioned sources of interference are evaluated in terms of the average optical power required at the receiver input to achieve a BER equal to $\text{BER}_{\text{target}}$, which is denoted by \bar{P}_{req} . In an ideal thermal noise-limited IM/DD system using M -PAM modulation with Gray coding, where errors between adjacent symbols are dominant, the BER is related to the received optical power by [54]

$$\text{BER} \approx \frac{2(M-1)}{M \log_2 M} Q \left(\sqrt{\frac{2 \log_2 M}{(M-1)^2} \frac{R^2 P_{\text{rec}}^2}{R_b N_0}} \right). \quad (5)$$

Let $\bar{P}_{M,\text{req}}$ denote the minimum power required for an ideal reference system using M -PAM. For the special case when $M = 2$, we denote the minimum optical power by $\bar{P}_{\text{OOK},\text{req}}$. Substituting in $\text{BER}_{\text{target}}$ and $M = 2$, the average optical power required to achieve $\text{BER}_{\text{target}}$ for an ideal OOK system is

$$\bar{P}_{\text{OOK},\text{req}} \approx \sqrt{\frac{R_b N_0}{2R^2}} Q^{-1}(\text{BER}_{\text{target}}). \quad (6)$$

Substituting the values located in Table I into (6) yields $\bar{P}_{OOK,req} \approx -14.6$ dBm. For reference, the RS for an ideal 4-PAM system is $\bar{P}_{4,req} \approx -11.4$ dBm.

To reduce the impact of the specific value chosen for the input-referred noise I_n on our analysis, the results are presented in terms of optical power penalty (OPP). The OPP is defined as the ratio of \bar{P}_{req} to $\bar{P}_{OOK,req}$.

It is often useful to compare the resulting OPP from an experiment to the OPP for an ideal reference system using M -PAM modulation. Ignoring the multiplicative factor in front of $Q(\cdot)$ in (5) and incorporating an additional power penalty due to a finite extinction ratio [21], the OPP for an ideal M -PAM system is

$$\frac{\bar{P}_{M,req}}{\bar{P}_{OOK,req}} = \frac{r_{ex} + 1}{r_{ex} - 1} \cdot \frac{M - 1}{\sqrt{\log_2 M}}. \quad (7)$$

To quantify the effectiveness of GS in reducing the impact of dispersion-induced signal-dependent distortion, we use a metric of dispersion tolerance, which we define as the total accumulated dispersion at which an additional OPP of 0.5 dB is incurred as compared to a zero-dispersion reference system. The zero-dispersion reference system has a design identical to the dispersion-impaired system except for at most two differences: (1) the accumulated dispersion is set to zero and (2) no GS is used in adjusting the transmitted intensity levels.

Using wavelengths longer and shorter than the zero-dispersion wavelength results in positive and negative accumulated dispersion, respectively. Thus, dispersion tolerance can in principle be defined using positive or negative accumulated dispersion. In this paper, we often consider negative dispersion values. In such cases, the improvement in dispersion tolerance, which is the difference between the dispersion tolerances with and without GS, is stated as a negative value.

IV. APPLICATION TO BANDWIDTH-CONSTRAINED INTRA-DATA CENTER LINKS

In this section, we evaluate the effectiveness of the proposed GS scheme in mitigating signal-dependent distortion in 200 Gb/s intra-DC links using M -PAM. We focus on two sources of signal-dependent distortion: (1) the combined bandwidth limitation and nonlinear transfer characteristic of the transmitter and (2) DD of an optical signal generated by a modulator with a positive linewidth enhancement factor.

We begin by presenting simulations with parameters chosen to isolate the effects of signal-dependent distortion arising from the nonlinear transfer characteristic and transmitter bandwidth limitations. We then present simulations studying the effect of GS on CD tolerance in systems using linear FFE. We conclude the section by studying the effect of GS on CD tolerance in systems using VNLE.

A. Transmitter Bandwidth Limitations and Linear Equalization

An important source of nonlinear distortion in IM/DD systems originates from the combined nonlinear transfer characteristic

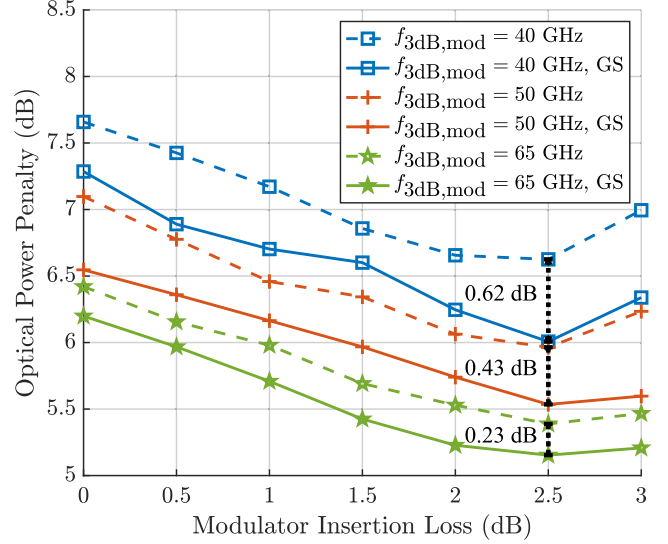


Fig. 4. Optical power penalty vs. modulator insertion loss using linear equalization for varying values of $f_{3\text{dB,mod}}$. The designation GS indicates that Algorithm 1 is used to optimize the drive voltage amplitudes. The system assumes $M = 4$, $V_{pp} = 2.5$ V, $I_d = 0$ nA, $f_{3\text{dB,DAC}} = f_{3\text{dB,PIN}} = \infty$, DAC resolution = ADC ENOB = ∞ , and accumulated dispersion = 0 ps/nm.

and bandwidth limitations of the transmitter. Owing to the nonlinear transfer characteristic $f_{\text{mod}}(\cdot)$ in (3), the mapping from output intensities $\{P_0, P_1, \dots, P_{M-1}\}$ to predistorted voltage amplitudes $\{V_0, V_1, \dots, V_{M-1}\}$ often results in unequally spaced voltage levels. The bandwidth limitations imposed before the nonlinear transfer characteristic cause signal-independent distortion to all predistorted voltage levels. However, the nonlinear transfer characteristic amplifies variations in the drive signal at voltage levels where the transfer characteristic's first derivative has a large magnitude. In addition, the nonlinear transfer characteristic attenuates variations in the drive voltage at voltage levels where its first derivative has a small magnitude. In our model, the nonlinear transfer characteristic converts signal-independent distortion to signal-dependent distortion.

For a fixed nonlinear transfer characteristic, the range of output intensity levels from the modulator is parameterized by V_{pp} and the modulator IL. When these two parameters are fixed, the uniform output intensity levels uniquely define a set of predistorted voltage amplitudes. The proposed GS scheme removes this constraint and determines an alternative set of output intensities subject to the output intensity range constraint. The effect of GS will thus depend on the choice of V_{pp} , the modulator IL, and $f_{3\text{dB,mod}}$.

Figs. 4 and 5 study how GS mitigates signal-dependent distortion arising from transmitter bandwidth limitations for varying values of V_{pp} and modulator IL. The other simulation parameters given in the caption are chosen to minimize other sources of signal-dependent noise and distortion.

We begin by fixing V_{pp} and varying the modulator IL and $f_{3\text{dB,mod}}$. Fig. 4 depicts the OPP vs. modulator IL for three different values of $f_{3\text{dB,mod}}$ with $V_{pp} = 2.5$ V and $M = 4$. We observe several important trends. First, across the entire ranges

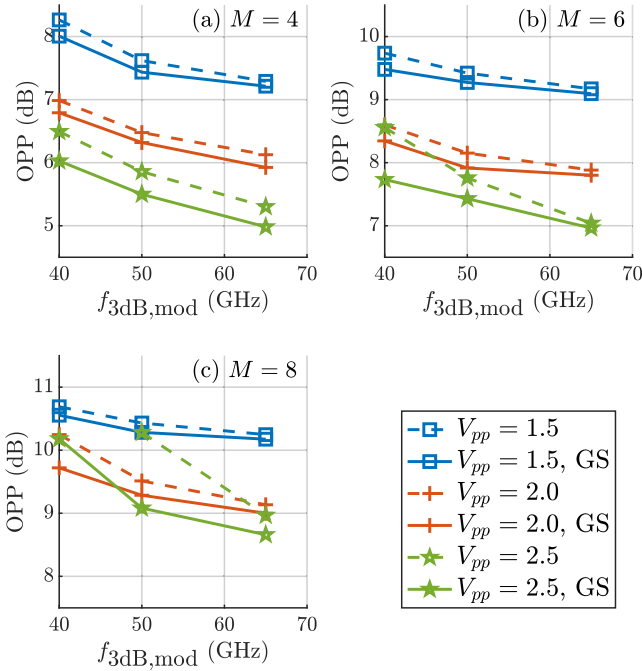


Fig. 5. Optical power penalty (OPP) vs. $f_{3\text{dB,mod}}$ using linear equalization for (a) $M = 4$, (b) $M = 6$, and (c) $M = 8$ and $V_{pp} = 1.5, 2$ or 2.5 V. The modulator insertion loss is set to 2.5 dB. The system assumes $I_d = 0$ nA, $f_{3\text{dB,DAC}} = f_{3\text{dB,PIN}} = \infty$, DAC resolution = ADC ENOB = ∞ , and accumulated dispersion = 0 ps/nm.

of modulator IL and M studied, GS provides an OPP improvement between 0.1 and 0.7 dB. Second, the OPP decreases monotonically until IL = 2.5 dB, above which the OPP increases. The insertion loss of 3 dB and $V_{pp} = 2.5$ V results in a driving voltage range that includes the upward-curving region of the nonlinear transfer characteristic. The lower values of OPP for higher values of modulator IL can be explained, in part, by an increase in r_{ex} , which can be observed in Fig. 2. Lastly, the reduction in OPP obtained using GS generally increases when stronger bandwidth constraints are imposed at the transmitter.

Fig. 5 studies how the reduction in OPP obtained using GS varies with the values of M and V_{pp} . The modulator IL is fixed to 2.5 dB because that value results in the lowest OPP in Fig. 4. We note that $M = 6$ is a two-dimensional modulation format employing a simple form of PS and is designed following [24].

The reduction in OPP obtained using GS varies with $f_{3\text{dB,mod}}$, M , and V_{pp} . The trend of larger OPP reductions for lower values of $f_{3\text{dB,mod}}$, first seen in Fig. 4, extends to other values of M and V_{pp} . In addition, the reduction in OPP is higher for $M = 8$ than for $M = 4$, owing to more closely spaced constellation points for $M = 8$. The OPP reduction for $M = 6$ is similar to that for $M = 4$, which is in part due to the PS inherent in the modulation format. Lastly, OPP reduction by GS increases as V_{pp} increases, because a higher V_{pp} results in a higher r_{ex} , which generally leads to increased distortion when using uniform intensity levels.

Among the three modulation orders studied, $M = 4$ provides the best RS for all values of $f_{3\text{dB,mod}}$ and V_{pp} studied. This finding is consistent with [55], [56], which found that 4-PAM outperforms 6-PAM at the KP4-FEC BER threshold. It is important

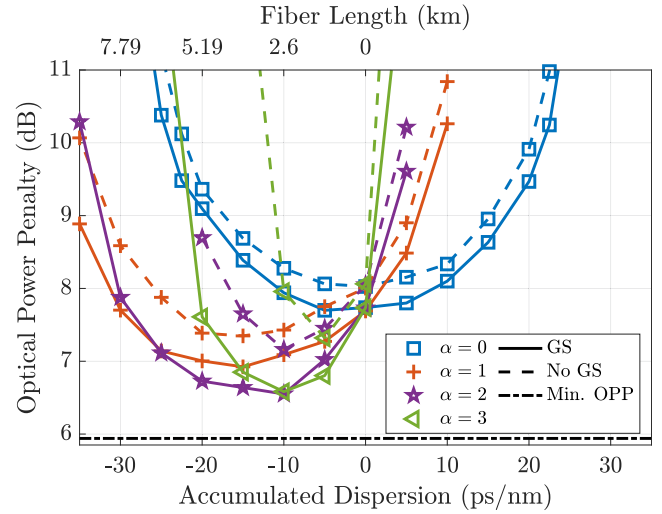


Fig. 6. Optical power penalty vs. accumulated dispersion using linear equalization for $M = 4$ and varying values of α . The remaining simulation parameters are $V_{pp} = 2$ V, modulator IL = 0 dB, $f_{3\text{dB,mod}} = 50$ GHz, $I_d = 0$ nA, $f_{3\text{dB,DAC}} = f_{3\text{dB,PIN}} = \infty$, and DAC resolution = ADC ENOB = ∞ .

to emphasize that this finding is specific to the use of an error correction code with pre-FEC BER of 1.8×10^{-4} . Using an alternative FEC scheme with a sufficiently high threshold BER, higher-order modulation formats may yield a lower OOP than $M = 4$.

B. Chromatic Dispersion and Linear Equalization

Signal-dependent distortion from the interaction between modulator chirp and CD has become an important design consideration for IM/DD transmission beyond 100 Gb/s per wavelength. In fact, the power penalty from CD may render 200 Gb/s-per-wavelength transmission impractical for intra-DC links beyond 2 km [56]. In this subsection, we study the effect of GS in mitigating this form of signal-dependent distortion, focusing on 200 Gb/s-per-wavelength links. We first study the impact of modulator chirp on the OPP and show that GS can reduce the effect of chirp. We then consider higher-order modulation and examine how increasing M impacts OPP and CD tolerance in systems employing GS and linear FFE.

1) *Modulator Chirp*: It is well-known that a nonzero modulator linewidth enhancement factor causes the OPP to differ between negative and positive values of accumulated dispersion [22], [35], [57]. For positive values of α , negative dispersion causes the transmitted pulses to narrow initially while propagating through the fiber. This results in an initial decrease in OPP for small negative values of accumulated dispersion relative to zero accumulated dispersion.

The impact of accumulated dispersion on OPP depends on the sign and magnitude of the accumulated dispersion and α . Fig. 6 shows the OPP vs. accumulated dispersion for $M = 4$ and various values of α . For positive values of accumulated dispersion, the OPP increases monotonically with increasing values of both the accumulated dispersion and α . GS reduces

the OPP by several tenths of a decibel at each accumulated dispersion value tested.

The relationship among OPP, α , accumulated dispersion, and GS is more complicated in the regime of positive α and negative accumulated dispersion. As the accumulated dispersion decreases from zero toward larger negative values, the OPP initially decreases and then increases. The expected initial decrease in OPP is consistent with the initial pulse narrowing expected for positive values of α and sufficiently low values of the accumulated dispersion. Increasing α in this regime initially causes the minimum OPP to occur at more negative values of accumulated dispersion. For sufficiently high values of α , the OPP minimum tends toward 0 ps/nm. GS causes the OPP minimum to shift to a larger negative accumulated dispersion for the three positive values of α shown. The relationships outlined here are consistent with industry results presented in [57].

The extent to which the CD-induced distortion is signal-dependent is an increasing function of α over the range of α values studied. When $\alpha = 0$, the CD-induced distortion is largely signal-independent. This can be seen in an almost constant OPP gap between a system using GS and a system not using GS at all accumulated dispersion values. For negative accumulated dispersion values and positive chirp values, the OPP gap resulting from GS increases monotonically with increasing modulator chirp. In addition, for constant α , the OPP gap between the OPP minima when using GS and uniform spacing grows larger as α increases.

Fig. 6 shows that the GS scheme enables IM/DD links to tolerate higher levels of modulator chirp. For example, at an accumulated dispersion of -25 ps/nm, an error floor occurs at $\alpha = 2$ when uniform spacing is used. For the optimized level spacing, the GS scheme ameliorates the impact of chip and chromatic dispersion and allows the system to operate with lower OPP than at zero accumulated dispersion.

2) *Higher-Order Modulation*: Increasing the modulation order affects at least two relevant parameters that directly impact the dispersion tolerance of an IM/DD system. For a given choice of r_{ex} , R_b , and average transmitted power, increasing the modulation order M decreases the distance between adjacent symbols in the constellation, thereby decreasing the total amount of distortion the system can tolerate. However, increasing M reduces the bandwidth occupied by the signal, thereby decreasing the impact of CD on the transmitted signal.

We now examine how OPP varies with increasing dispersion and GS for different values of M . Fig. 7 shows the OPP vs. accumulated dispersion for $M = 4, 6, \text{ and } 8$. The resulting dispersion tolerance for each of the six cases is depicted by a solid dot, and the minimum OPP is also provided as a reference. The modulator IL is set to 0 dB to allow for future increases in V_{pp} without changing the modulator IL. The remaining parameters are chosen to minimize sources of distortion other than CD.

The proposed GS scheme increases dispersion tolerance by -12.71 , -30.48 , and -17.18 ps/nm for $M = 4, 6, \text{ and } 8$, respectively. The modulation order $M = 4$ provides the lowest OPP for any dispersion level for uniform spacing and for dispersion values less than -32 ps/nm for GS, respectively. $M = 6$ provides the highest overall dispersion tolerance and a lower

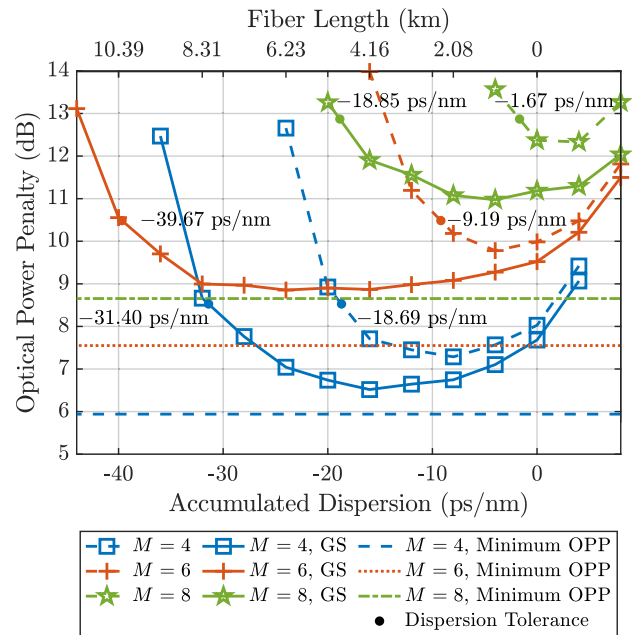


Fig. 7. Optical power penalty (OPP) vs. accumulated dispersion using linear equalization for $M = 4, 6, \text{ and } 8$. The top x-axis indicates the corresponding fiber length assuming a laser wavelength of 1270 nm. The solid dot on each marked line indicates the linearly extrapolated dispersion tolerance. The unmarked lines indicate the approximate minimum OPP given a fixed modulation format and finite extinction ratio. The other variable simulation parameters are $V_{pp} = 2$ V, modulator IL = 0 dB, $f_{3\text{dB,mod}} = 50$ GHz, $\alpha = 2$, $I_d = 0$ nA, $f_{3\text{dB,DAC}} = f_{3\text{dB,PIN}} = \infty$, and DAC resolution = ADC ENOB = ∞ .

overall OPP for dispersion levels greater than -32 ps/nm. Both the dispersion tolerance and OPP for $M = 8$ are substantially worse than for the other modulation formats.

The effect of the proposed GS scheme differs for positive and negative values of accumulated dispersion. The distortion arising from positive accumulated dispersion is less signal-dependent than for negative accumulated dispersion. The effect of this asymmetry can be seen in Figs. 6 and 7 as a smaller OPP reduction between the uniform spacing and GS curves for positive dispersion than for negative dispersion.

We now study how the optimized intensity levels vary with accumulated dispersion under the proposed GS scheme. Fig. 8 shows the normalized output power vs. accumulated dispersion from Fig. 7 for $M = 8$ with GS. The proposed GS scheme changes the optimized intensity levels more for negative dispersion values than for positive dispersion values. The combined effects of negative dispersion and positive α lead to signal-dependent distortion at higher normalized intensity levels, an effect observed experimentally in [34]. The proposed GS scheme compensates for this effect by shifting the higher intensity levels to lower values. The magnitude of this downward shift increases with decreasing accumulated dispersion. Lastly, we note that the effect of GS in the absence of chromatic dispersion can be inferred by examining the transmitted intensities at zero dispersion.

The impact of signal-dependent distortion for negative or positive dispersion values can be observed in Fig. 8. At an accumulated dispersion of -16 ps/nm, the proposed GS scheme

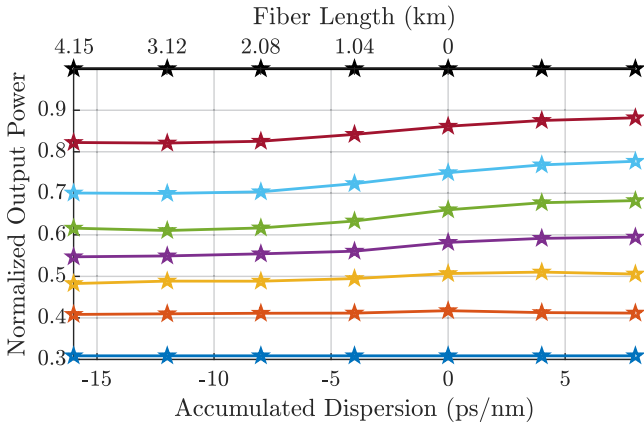


Fig. 8. Normalized output power vs. accumulated dispersion from Fig. 7 for $M = 8$ using linear equalization and GS. The normalized output power is obtained by dividing the power of each signal point by the power of the highest amplitude signal point. The signal-to-noise ratio is scaled so that the achieved BER \approx BER_{target}. The top x-axis indicates the corresponding fiber length assuming a laser wavelength of 1270 nm. The normalized output power is given by $10^{(-\alpha_{dB}(V(t))/10)}$. The other simulation parameters are the same as those used in Fig. 7.

shifts the second, third, and fourth highest output powers to lower values. By contrast, at an accumulated dispersion of +8 ps/nm, GS shifts these three intensity levels upward. We note that the case of positive α and negative dispersion is of particular interest in intra-DC CWDM links, as some WDM standards use wavelengths shorter than the zero-dispersion wavelength [25]. Because of this observed asymmetry and consistent with the choice of CWDM wavelengths, the remainder of our study assumes negative accumulated dispersion values.

The modulator extinction ratio r_{ex} is another important design parameter in IM/DD links due to its impact on two other important physical quantities. For a fixed M , increasing r_{ex} results in a larger distance between signal points in a constellation, thereby improving noise tolerance and RS in the absence of other effects. However, increasing the modulator extinction ratio also increases the difference between the highest and lowest output powers, which exacerbates the phase modulation due to transient chirp. The results in Figs. 7 and 8 are obtained for fixed r_{ex} , which has so far prevented any analysis on the impact of r_{ex} on dispersion tolerance. To study the net effect of increasing r_{ex} in distortion-limited IM/DD links, we examine how the dispersion tolerance changes as a function of extinction ratio in systems using either uniform spacing or GS.

Fig. 9 shows the dispersion tolerance for different combinations of extinction ratio and modulation order. The insertion loss is fixed to 0 dB to ensure that as r_{ex} is varied, a similar range of the transfer characteristic is used. In most cases studied, increases in r_{ex} are associated with decreasing values of the dispersion tolerance. Therefore, over the range of extinction ratios studied, the negative impact of greater chirp-induced phase modulation outweighs the positive impact of increased signal spacing on dispersion tolerance. The combination of $M = 8$ with GS yields equal dispersion tolerances for $V_{pp} = 2$ and 2.5 V, because the effect of increased chirp-induced signal-dependent distortion is negated by the larger extinction ratio and GS.

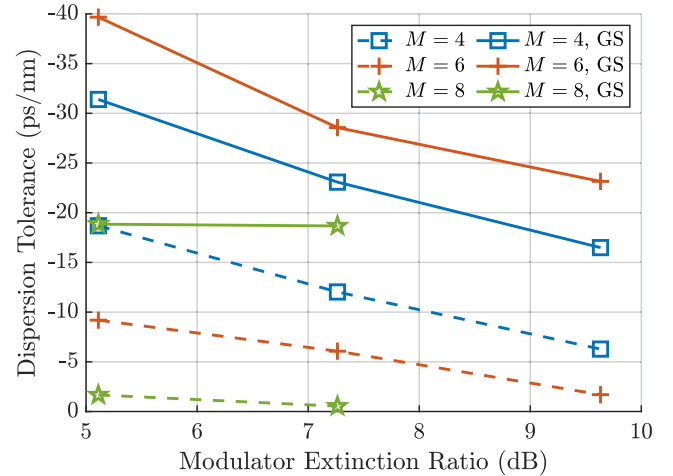


Fig. 9. Dispersion tolerance vs. modulator extinction ratio using linear equalization for $M = 4, 6,$ and 8 . From left to right, the simulated modulator extinction ratios correspond to $V_{pp} = 2, 2.5,$ and 3 V. The remaining simulation parameters are modulator IL = 0 dB, $f_{3dB,mod} = 50$ GHz, $\alpha = 2$, $I_d = 0$ nA, $f_{3dB,DAC} = f_{3dB,PIN} = \infty$, and DAC resolution = ADC ENOB = ∞ .

We also note that the dispersion tolerance increase obtained using GS is smaller for $V_{pp} = 2.5$ or 3 V than $V_{pp} = 2$ V. For $V_{pp} > 2$ V, the largest improvements in dispersion tolerance from GS are -11.1 ps/nm and -22.5 ps/nm for $M = 4$ and $M = 6$, respectively. For $V_{pp} = 2$ V, the improvements in dispersion tolerance from GS are -12.7 ps/nm and -30.48 ps/nm for $M = 4$ and $M = 6$, respectively.

The modulation scheme providing the largest dispersion tolerance depends on whether or not GS is used. When using conventional uniform spacing, $M = 6$ results in a lower dispersion tolerance than $M = 4$. Under uniform spacing, moving from $M = 4$ to $M = 6$ causes the upper constellation points to move closer together, which outweighs the benefits of reduced signal bandwidth occupation. By contrast, when the proposed GS scheme is used, $M = 6$ results in the largest dispersion tolerance among the modulation orders examined. For high levels of CD, the proposed GS scheme shifts the transmitted intensity levels downward, partially ameliorating some of the impact from the larger number of constellation points. Therefore, we conclude that the proposed GS scheme can change the value of M that yields the largest dispersion tolerance.

We observe in Fig. 9 that the accumulated dispersion tolerance varies substantially as a function of r_{ex} over the range of values studied. In addition, the parameter ranges studied were chosen to reflect values specified by IEEE standards [25], [58] and available in commercial components [23]. Thus, in the design of 200 Gb/s IM/DD systems, the choice of r_{ex} can strongly influence the impact of signal-dependent distortion arising from CD, depending on the fiber lengths considered.

C. Chromatic Dispersion and Volterra Nonlinear Equalization

In Secs. IV-A and IV-B, we showed that the proposed GS scheme reduces the impact of signal-dependent distortion in IM/DD links using linear FFE, yielding improved RS and CD

tolerance. Algorithm 1 improves system performance by adjusting the transmitted intensity levels according to the residual signal-dependent distortion after equalization is applied to the received signal. Because the algorithm operates on the observed error statistics at the receiver, the proposed GS scheme can be used in conjunction with various pre-distorters and equalizers. We assumed a linear FFE in Secs. IV-A and IV-B owing to its widespread use in intra-DC links [26]. Other possible nonlinear predistortion schemes include a Volterra series or Tomlinson-Harashima precoding. Decision-feedback equalization, MLS, or VNLE can also be used in lieu of linear FFE.

The joint design of VNLE and GS is of particular interest, as VNLE has been widely studied for mitigating nonlinear distortions in intra-DC IM/DD links [3], [28], [59], [60], [61], often in combination with other DSP techniques [59]. VNLE increases the maximum transmission distance and improves RS in IM/DD optical links at the expense of increased DSP complexity relative to linear FFE. VNLE improves performance by mitigating nonlinear distortions such as modulator chirp and CD. We have thus far found that the proposed GS scheme can improve RS and CD tolerance in IM/DD systems using linear FFE. We have not yet studied whether similar improvements can be obtained in systems using stronger forms of equalization, such as VNLE.

In this subsection, we study how improvements in RS and CD tolerance provided by GS change with an increasing memory length of the VNLE kernel. We limit our study to a second-order VNLE because the signal-dependent distortion arising from modulator chirp and CD are primarily second-order nonlinearities [3]. All subsequent references to VNLE presume a second-order VNLE. We begin by fixing the modulation order and varying the number of second-order taps $n_{\text{taps},2}$ and the linewidth enhancement factor α . We then extend the analysis to higher modulation orders.

1) *Modulator Chirp*: The combination of modulator chirp and CD induces signal-dependent distortion in the received electric field. The exact characteristics of the modulator chirp are dependent on the choice of a modulator. Adiabatic chirp and transient chirp are typically the dominant sources of spurious phase modulation in directly modulated lasers and EAMs, respectively [22], [34]. While our analysis focuses on transient chirp in EAMs, our proposed scheme could also be applied to DML-based IM/DD links, which also exhibit substantial signal-dependent distortion [61].

Fig. 10(a)–(c) show the OPP vs. accumulated dispersion with $M = 4$ and varying values of α . Fig. 10(a), (b), and (c) assume $\alpha = 1, 2$, and 3, respectively. The line marker and color combination in the bottom legend applies to all three subfigures. The other design parameters are chosen to simplify the model and to focus on the effects of modulator chirp and chromatic dispersion.

The proposed GS scheme reduces the OPP for all accumulated dispersion values and all VNLE memory lengths. In general, the absolute improvement in CD tolerance is higher when a smaller number of VNLE taps is used. GS provides the largest absolute increase in CD tolerance when using linear FFE for $\alpha = 1$ and 2. GS provides the largest increase in CD tolerance for the 3-tap

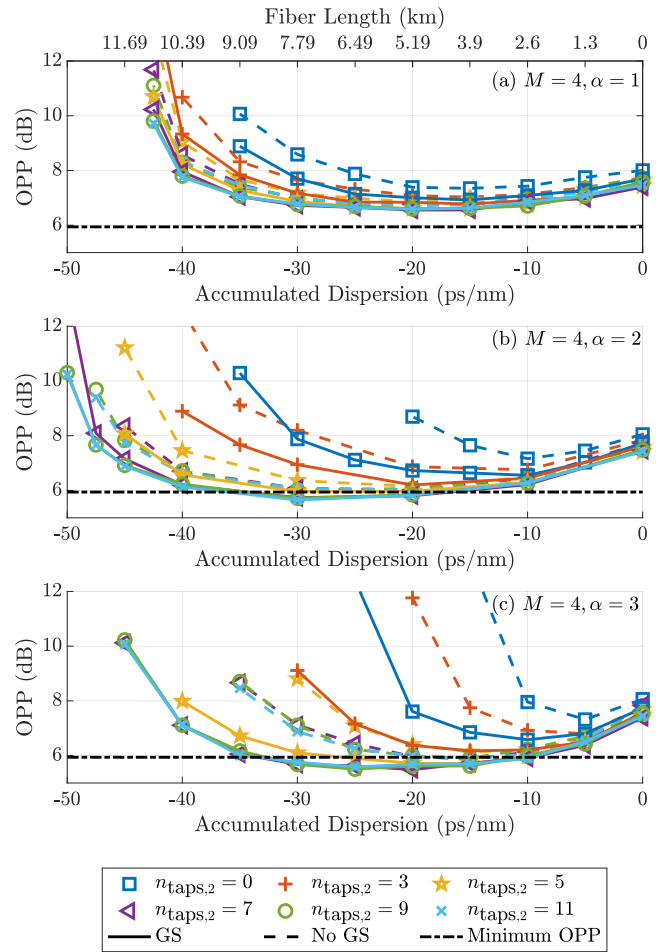


Fig. 10. Optical power penalty (OPP) vs. accumulated dispersion for $M = 4$, varying the number of second-order Volterra taps $n_{\text{taps},2}$, for (a) $\alpha = 1$, (b) $\alpha = 2$, and (c) $\alpha = 3$. The legend is common to all three subfigures. The numeric values in the legend indicate the number of 2nd-order Volterra taps used. The top x-axis indicates the corresponding fiber length assuming a laser wavelength of 1270 nm. The other variable simulation parameters are $V_{pp} = 2$ V, modulator IL = 0 dB, $f_{3\text{dB},\text{mod}} = 50$ GHz, $I_d = 0$ nA, $f_{3\text{dB},\text{DAC}} = f_{3\text{dB},\text{PIN}} = \infty$, and DAC resolution = ADC ENOB = ∞ .

VNLE when $\alpha = 3$. For a VNLE memory length of 7 or higher and $\alpha = 1$ or 2, GS provides a CD tolerance increase of several ps/nm. In the case of $\alpha = 3$, a larger CD tolerance improvement is observed for a VNLE memory length of at least 7 or more.

The RS achieved using GS and 21-tap linear FFE is similar to that using uniform level spacing and VNLE with 21 linear and 3 nonlinear taps. In Fig. 10(a) and (b), GS with linear FFE and uniform level spacing with 3-tap VNLE achieve almost identical optical power penalties for accumulated dispersion values down to -30 ps/nm. GS with linear FFE is subject to a higher OPP for values below -30 ps/nm. In Fig. 10(c), GS with linear FFE outperforms uniform level spacing with 3-tap VNLE at all accumulated dispersion values.

The relationship between CD tolerance and modulator chirp varies depending on the choice of VNLE memory and intensity level spacing. For linear FFE with GS, linear FFE with GS, and 3-tap VNLE without GS, the CD tolerance decreases monotonically as α increases. For all other combinations of VNLE

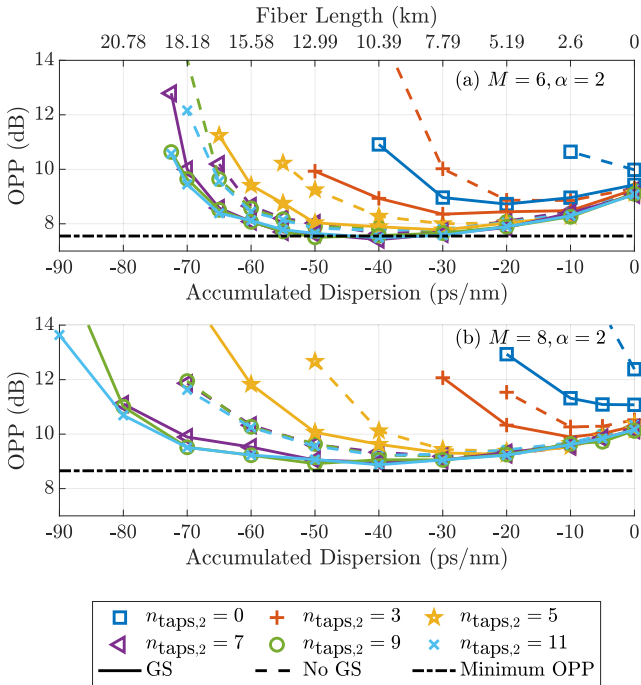


Fig. 11. Optical power penalty (OPP) vs. accumulated dispersion for $\alpha = 2$, varying the number of second-order Volterra taps, for (a) $M = 6$ and (b) $M = 8$. The legend is common to both figures. The numeric values in the legend indicate the number of 2nd-order Volterra taps used. The top x-axis indicates the corresponding fiber length assuming a laser wavelength of 1270 nm. The other variable simulation parameters are $V_{pp} = 2$ V, modulator IL = 0 dB, $f_{3\text{dB},\text{mod}} = 50$ GHz, $I_d = 0$ nA, $f_{3\text{dB},\text{DAC}} = f_{3\text{dB},\text{PIN}} = \infty$, and DAC resolution = ADC ENOB = ∞ .

memory and level spacing, the CD tolerance initially increases when α changes from 1 to 2, and then decreases when $\alpha = 3$.

The increase in CD tolerance obtained using GS is generally larger for higher values of α . For almost all choices of VNLE memory length, the increase in CD tolerance obtained using GS is largest for $\alpha = 3$ and larger for $\alpha = 2$ than $\alpha = 1$. A notable exception is for linear FFE, where the increase in CD tolerance obtained using GS is largest for $\alpha = 2$.

We do not plot the case when $\alpha = 0$ to simplify Fig. 10. Including $\alpha = 0$ would not yield substantial insight, as both the VNLE and GS provide almost no improvement in CD tolerance. An error floor occurs before -30 ps/nm for all combinations of VNLE memory and GS studied. We note that the linear FFE with GS and 3-tap VNLE provide almost identical performance when $\alpha = 0$.

2) *Higher-Order Modulation*: Increasing constellation density has two important effects on CD tolerance. For a fixed data rate, increasing M decreases the bandwidth occupied by the signal, thereby decreasing CD-induced signal-dependent distortion. The increased density of constellation points also increases the system's sensitivity to a given level of signal-dependent distortion, owing to a reduced distance between adjacent constellation points.

Fig. 11(a) and (b) show OPP vs. accumulated dispersion for $\alpha = 2$ and varying values for M . Fig. 11(a) and (b) assume

$M = 6$ and 8, respectively. The case of $M = 4$ and $\alpha = 2$ is shown in Fig. 10(b).

The impact of GS on CD tolerance varies with the modulation order used. For $M = 4$ and $M = 6$, the increase in CD tolerance from GS is the largest for linear FFE and decreases with increasing VNLE memory length. For $M = 8$, by contrast, GS provides a consistent ~ 10 -15 ps/nm increase in CD tolerance for all VNLE memory lengths.

The relationship between modulation order and CD tolerance is dependent on the combination of VNLE memory and GS. For linear FFE with GS, linear FFE without GS, and 3-tap VNLE without GS, increasing the modulation order from $M = 4$ to $M = 6$ results in decreased CD tolerance. For the three aforementioned cases, 3-tap VNLE with GS, and 5-tap VNLE without GS, increasing the modulation order from $M = 6$ to $M = 8$ leads to decreased CD tolerance. The CD tolerance for a system using a 7-, 9-, and 11-tap VNLE increases monotonically with increasing modulation order, whether or not GS is used.

Given cost and complexity constraints in IM/DD links, the comparative performance of linear FFE with GS against a VNLE without GS is of particular interest. Fig. 10(b) shows that for $M = 4$ and $\alpha = 2$, a linear FFE with GS and a 3-tap VNLE without GS deliver similar CD tolerances. Fig. 11(a) shows that for $M = 6$ and $\alpha = 2$, a system employing a linear FFE with GS has a higher CD tolerance than a system employing a 3-tap VNLE without GS. By contrast, Fig. 11(b) shows that for $M = 8$ and $\alpha = 2$, the 3-tap VNLE without GS enables a higher CD tolerance than the linear FFE with GS. These results highlight the ability of GS to improve CD tolerance when lower-order modulation is used and the necessity of VNLE (or perhaps other nonlinear equalization techniques) when employing denser transmit constellations.

V. IMPLEMENTATION CONSIDERATIONS

In this section, we address issues for implementing the proposed GS scheme in 200 Gb/s-per-wavelength links. We first study the data converter resolution required to support GS. We then study drive signal design for the highest-dispersion channel in an intra-DC CWDM system with GS and present the implications for per-channel optimization in WDM systems. Finally, we discuss options for estimating the conditional error probabilities and adjusting the transmitted intensity levels to implement the proposed GS scheme.

For the remainder of Section V, we assume linear FFE and a modulation order $M = 4$. These choices are motivated by several results from Section IV. The choice of linear FFE is motivated by the strong complexity constraints in intra-DC links. For linear FFE, Fig. 5 shows that $M = 4$ results in the lowest OPP for all choices of $f_{3\text{dB},\text{mod}}$ and V_{pp} studied. While Fig. 7 shows that $M = 4$ provides less maximum dispersion tolerance than $M = 6$ when using GS, $M = 4$ with GS can provide a dispersion tolerance greater than -24 ps/nm with a reasonable V_{pp} . For these reasons, $M = 4$ with linear FFE is seen to be a suitable combination.

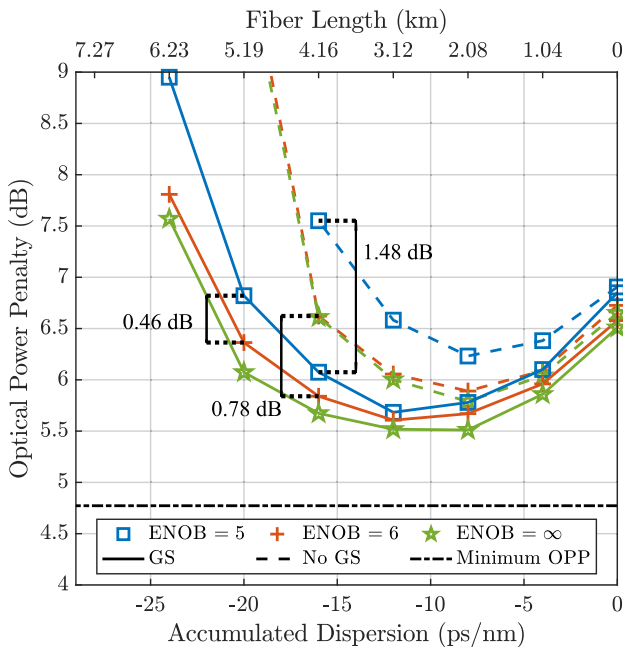


Fig. 12. Optical power penalty vs. accumulated dispersion using linear equalization for ENOB = 5, 6, and ∞ . The solid dot on each marked line indicates the linearly extrapolated dispersion tolerance. The unmarked horizontal line indicates the approximate minimum OPP for $M = 4$ and $r_{ex} = 7.4$ dB. The top x-axis indicates the corresponding fiber length assuming a laser wavelength of 1270 nm. The other simulation parameters are $V_{pp} = 2$ V, modulator IL = 2.5 dB, $f_{3dB,mod} = f_{3dB,DAC} = f_{3dB,PIN} = 65$ GHz, $\alpha = 2$, $I_d = 10$ nA, and DAC resolution = ADC ENOB.

A. DAC and ADC Requirements

High-bandwidth data converters, including DACs and ADCs [62], enable various DSP algorithms at the transmitter and receiver, for mitigating key impairments in intra-DC links [3]. However, data converters and associated DSP algorithms are sources of substantial power consumption in intra-DC links [62]. It is therefore important to assess the DAC resolution and ADC effective number of bits (ENOB) required by the proposed GS scheme.

In addition to using finite quantization at the ADC and DAC, we adjust other component parameters to reflect modern intra-DC links. We set the PIN dark current to 10 nA [22], [63]. Following [64], we model the bandwidth limitations in the system by setting $f_{3dB,mod} = f_{3dB,DAC} = f_{3dB,PIN}$. This removes several degrees of freedom in choosing various component parameters while closely approximating the overall frequency response for many other choices of component bandwidth limitations. For similar reasons, we also assume that the DAC resolution and ADC ENOB are equal.

Fig. 12 shows the OPP vs. accumulated dispersion for ADC ENOB = 5, 6, and ∞ . For both GS and uniform intensity levels, increasing DAC and ADC resolutions from 5 to 6 b decreases the OPP over the entire range of accumulated dispersion studied. An additional decrease in OPP is observed at ENOB = ∞ as compared to ENOB = 6 b, but the decrease is smaller. We note that the total dispersion tolerance here is higher than the $M = 4$ simulation depicted in Fig. 7. This is due, in part,

to the additional bandwidth limitations of the DAC and PIN photodetector, which substantially reduce the bandwidth of the end-to-end system [64].

We now examine the OPP reduction resulting from GS for fixed data converter resolutions. Fig. 12 explicitly indicates the reductions in OPP at -16 ps/nm for ENOB = 5 and 6 b obtained using GS, which are 1.48 and 0.78 dB, respectively. GS is seen to yield a larger decrease in OPP over uniform spacing for ENOB = 5 b than for ENOB = 6 b, a trend that holds for other values of accumulated dispersion as well.

We alternatively study the relative OPP reduction resulting from increasing data converter resolution for a given level spacing scheme. At an accumulated dispersion of -20 ps/nm in Fig. 12, an increase in data converter resolution from 5 to 6 b decreases the OPP by 0.46 dB when GS is used. An error floor occurs when ENOB = 5 b at -20 ps/nm so an OPP improvement cannot be stated when uniform spacing is used. These improvements can be attributed, in part, to GS compensating for higher levels of signal-dependent distortion arising from quantization when ENOB = 5 b. We conclude that GS can be exploited to decrease the impact of quantization noise arising from low data converter resolutions.

B. Drive Signal Design in WDM Systems

In this section, we optimize the parameters of the drive signal to optimize the RS of the most dispersion-impaired wavelength in a WDM system. We jointly optimize the following three parameters of the drive signal: V_{pp} , insertion loss, and the inner drive signal levels via GS. We compute the OPP difference between a system that optimizes all three parameters and an equivalent system that optimizes V_{pp} and insertion loss but uses uniform intensity levels. We show that the optimal value of V_{pp} varies widely as a function of the accumulated dispersion and discuss the implications this has on drive signal design in WDM systems with substantial dispersion. We use intra-DC CWDM as a design example and assume the corresponding wavelengths and fiber lengths to provide a concrete and practically relevant set of system parameters. Our optimization procedure, however, can be easily extended to other WDM systems.

Recent IEEE standards for CWDM have adopted either four or eight wavelengths near the zero-dispersion wavelength [25]. Considering eight wavelengths, the 1270 nm wavelength will incur the largest negative accumulated dispersion. According to (1), the dispersion parameter at 1270 nm is -3.85 ps/(nm \cdot km). Conservatively rounding to -4 ps/(nm \cdot km) and assuming fiber lengths of 2 and 6 km, the most negative accumulated dispersion values in our CWDM design example are approximately -8 and -24 ps/nm, respectively. For simplicity, we perform optimization only for accumulated dispersion levels of -8 and -24 ps/nm, but our optimization could also be performed for the other wavelengths in a CWDM system.

In our model and assuming $M = 4$, there are three remaining degrees of freedom in the design of the transmitted intensity levels. Assuming equal intensity level spacing, the two remaining design parameters are the peak-to-peak voltage and the modulator insertion loss. The proposed GS scheme removes the

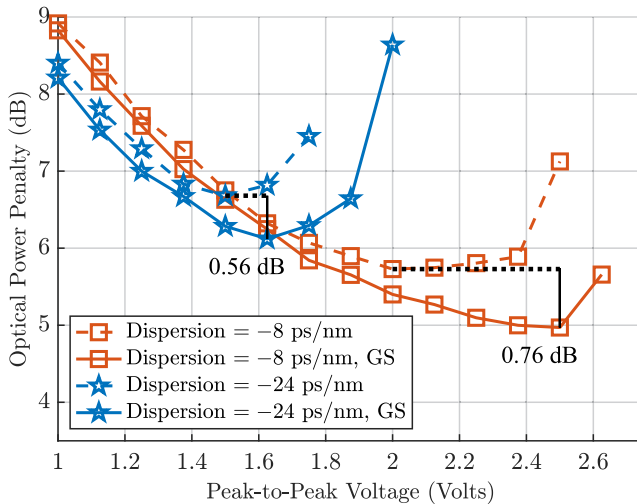


Fig. 13. Optical Power Penalty vs. peak-to-peak voltage using linear equalization for accumulated dispersion = -8 and -24 ps/nm. The other simulation parameters are modulator IL = 2.5 dB, $f_{3\text{dB,mod}} = f_{3\text{dB,DAC}} = f_{3\text{dB,PIN}} = 50$ GHz, $\alpha = 2$, $I_d = 10$ nA, and DAC resolution = ADC ENOB = 6 b.

uniform spacing constraint, allowing for an optimized design of the inner intensity levels.

Independent optimization of each of the three design parameters mentioned above can yield a suboptimal solution, as varying one parameter can affect the optimal values of the other two. Increasing the peak-to-peak voltage is desirable, as it increases the extinction ratio, thereby lowering the theoretical minimum OPP as described in (6). However, increasing the extinction ratio reduces dispersion tolerance, as shown in Fig. 9. The choice of modulator insertion loss is equivalent to choosing the interval of the nonlinear transfer characteristic being used, thereby affecting transmitter bandwidth-induced signal-dependent distortion and modulator extinction ratio.

Fig. 13 shows OPP vs. peak-to-peak voltage using linear equalization for accumulated dispersion values of -8 and -24 ps/nm. Because intra-DC links are often subject to strict peak-to-peak drive voltage constraints, we bias the modulator at -2.5 dB, which is the optimum value found in Fig. 4 and is near the maximum-extinction-ratio region of the modulator nonlinear transfer characteristic. We also fix DAC resolution = ADC ENOB = 6 b, which we showed in Section V-A is sufficient to provide near-optimal performance. We can optimize the peak-to-peak voltage by selecting the value that minimizes the OPP. The difference between the minimum OPPs for the two systems is depicted in the figure and quantifies the OPP reduction provided by the proposed GS scheme.

For an accumulated dispersion of -24 ps/nm, as V_{pp} increases, the OPP decreases until the minima at $V_{pp} = 1.5$ V and $V_{pp} = 1.625$ V when using uniform spacing and GS, respectively, above which the OPP increases monotonically. For an accumulated dispersion of -8 ps/nm, the minimum OPP values are achieved at $V_{pp} = 2$ V with uniform spacing and $V_{pp} = 2.5$ V with GS. The OPP is at least 1.5 dB lower at the optimal values of V_{pp} as compared to $V_{pp} = 1$ V for all combinations of accumulated dispersion and level spacing design.

Using GS leads to additional reductions in the minimum OPP of 0.76 dB and 0.56 dB for accumulated dispersion values of -8 and -24 ps/nm, respectively.

In an IM/DD WDM system, where different channels are subject to different values of accumulated dispersion, the optimal value for V_{pp} can vary substantially between channels. For example, in a 6 km WDM system, channels at wavelengths of 1296 and 1270 nm will be subject to accumulated dispersion values of approximately -8 ps/nm and -24 ps/nm, respectively. According to Fig. 13, the optimized values of V_{pp} for the two wavelengths will differ by as much as 1 V. Therefore, a WDM system using CWDM wavelengths will achieve a better RS by optimizing V_{pp} for each wavelength separately as compared to an equivalent system that uses the same value of V_{pp} for each wavelength. Jointly optimizing V_{pp} and the inner intensity levels using GS further improves RS for each channel.

1) *Digital Pulse Shaping*: The overall end-to-end system bandwidth can have an important impact on the dispersion tolerance of an IM/DD system [64]. Digital pulse shaping for bandwidth-limited IM/DD channels is one possible method for reducing signal bandwidth and has been studied for several decades [21], [65], [66].

Digital pulse shaping can modify several physical properties of the transmitted signal, which can have both positive and negative effects on RS and CD tolerance. Digital pulse shaping can be used for signal bandwidth compression and digital pre-distortion, which should improve both RS and CD tolerance absent other factors. However, digital pulse shaping for IM signals has been shown to increase the peak value of the signal, which can exacerbate chirp-induced phase modulation. In addition, the unipolar constraint of IM signals may require the addition of a DC bias, which can result in an OPP of several dB [21].

The drive signal design procedure presented in Section V-B jointly optimized V_{pp} , insertion loss, and inner drive signal levels and did not consider digital pulse shaping. Similar to other properties of the drive signal analyzed, we expect that digital pulse shaping would have an impact on RS and CD tolerance in an IM/DD system using GS. We consider our omission of digital pulse shaping appropriate in the context of intra-DC interconnects, where DAC-less transmitter designs are often used [27], [67]. The joint design of digital pulse shaping and GS for IM/DD links is an interesting topic for future work.

C. Intensity Level Computation and Adjustment

In this section, we discuss how to estimate the conditional symbol-error probabilities $p_{j,+}$ and $p_{j,-}$, compute the updated intensity levels, and adjust the transmitted intensity levels in order to implement Algorithm 1.

A straightforward implementation of Algorithm 1 requires a mechanism to estimate the post-equalization symbol-error statistics (SES) at the receiver, computation of the updated intensity levels, and a mechanism for feedback from the receiver to the transmitter. GS schemes that use SES at the receiver can be collectively referred to as GS-SES. SES could be estimated periodically by transmitting a known sequence or by exploiting

the syndrome computed in the error-correction decoder. Computation of the updated intensity levels could be performed at either the transmitter or receiver. Implementations using SES measured at the receiver to compute the updated intensity levels will require feedback of either the SES or the updated intensity levels to the transmitter, depending on whether the computations are performed at the transmitter or receiver. However, feedback is not currently available in DC links, and may need to be adopted to support GS-SES.

There are several other factors to account for when considering GS schemes that use a feedback channel. The transmission latency for intra-DC links is on the order of tens of microseconds. The delay between the estimation of SES at the receiver and the intensity level updates at the transmitter may induce system instability depending on the coherence time of the channel. In addition, the proposed GS scheme can be used to trade off between the complexity associated with the GS scheme and receiver DSP complexity. The optimal trade-off between the complexity of a feedback channel and receiver DSP complexity may depend on other factors, such as the link budget, modulator chirp, modulation order, link length, baud rate, etc.

A feedback channel may not be strictly necessary to implement GS-SES. Offline modeling and static lookup tables may be employed to avoid requirements for SES estimation and a feedback channel. For example, pre-distortion based on offline modeling and lookup tables for 4-PAM IM/DD links has been investigated extensively [68], [69], [70]. Methods based on offline modeling, however, may be of limited effectiveness in situations where the model does not reliably represent the actual system. In addition, predistortion and GS schemes that avoid a feedback channel may need additional information about the channel, such as the link distance or bandwidth limitations.

A transmitter DAC provides one straightforward way to adjust the transmitted intensity levels. Using a DAC has the further benefit of enabling various DSP techniques that may be central to mitigating key sources of distortion in IM/DD links [3]. For example, [71] used a 4-b DAC, with 2 b dedicated to signal-dependent FFE and 2 b used for nonlinear predistortion. The nonlinear predistortion technique is similar to the proposed GS scheme and was designed offline to account for signal-dependent ISI resulting from modulator nonlinearity. The importance of reducing the impact of nonlinearity and bandwidth limitations from individual components is heightened as data rates are increased.

An electrical DAC at the transmitter may not be strictly necessary for adjusting the transmitted intensity levels. For example, previously demonstrated IM/DD [27], [67] and coherent transceivers [72] employed DAC-less transmitter designs while supporting the transmission of 4-level signals. These systems [27], [67], [72] encoded 4-PAM symbols using segmented electrodes and independent drive signals for the least and most significant bits. By adding an additional bias voltage section to the modulator, the transmitter in [27] supported dynamic adjustment of the transmitted intensity levels. Independent control of each intensity level could be achieved by using the differential encoding of the least and most significant bits, adjustable modulator bias voltages, and a dual-parallel modulator structure [73].

VI. CONCLUSION

A GS scheme that optimizes transmitted intensity levels to achieve substantially equal conditional error probabilities at all decision thresholds at the receiver was presented in this paper. The scheme was analyzed for its suitability in IM/DD intra-data center links, where signal-dependent distortion from bandwidth-limited, nonlinear components and chromatic dispersion limit system performance. The GS scheme was shown to improve RS and increase CD tolerance, while reducing the OPP caused by finite-resolution data converters over a wide range of channel parameters. The proposed scheme was found to improve RS by 0.76 dB and 0.56 dB at accumulated dispersion values of -8 ps/nm and -24 ps/nm, respectively, over an equivalent system using an optimized modulator extinction ratio, uniformly spaced constellation points, and LE. The proposed scheme can also be used to reduce the complexity of the DSP required to achieve a target RS and transmission reach, as evidenced by the similar performances achieved by a standard linear FFE with GS and a three-tap, second-order VNLE without GS. Key implementation issues and data converter resolution requirements for the proposed GS scheme were discussed.

ACKNOWLEDGMENT

Any opinions, findings, and conclusions or recommendations expressed here are those of the authors and do not necessarily reflect the views of the National Science Foundation.

REFERENCES

- [1] Q. Cheng, M. Bahadori, M. Glick, S. Rumley, and K. Bergman, "Recent advances in optical technologies for data centers: A review," *Optica*, vol. 5, no. 11, pp. 1354–1370, Nov. 2018. [Online]. Available: <http://opg.optica.org/optica/abstract.cfm?URI=optica-5-11-1354>
- [2] X. Zhou, R. Urata, and H. Liu, "Beyond 1 Tb/s intra-data center interconnect technology: IM-DD OR coherent?," *J. Lightw. Technol.*, vol. 38, no. 2, pp. 475–484, 2020.
- [3] K. Zhong, X. Zhou, J. Huo, C. Yu, C. Lu, and A. P. T. Lau, "Digital signal processing for short-reach optical communications: A review of current technologies and future trends," *J. Lightw. Technol.*, vol. 36, no. 2, pp. 377–400, Jan. 2018.
- [4] S. Kumar, G. Papen, K. Schmidtke, and C. Xie, "Chapter 14 - intra-data center interconnects, networking, and architectures," in *Opt. Fiber Telecommun. VII*, A. E. Willner Ed. New York, NY, USA: Academic Press, 2020, pp. 627–672. [Online]. Available: <https://www.sciencedirect.com/science/article/pii/B9780128165027000166>
- [5] Z. Qu and I. B. Djordjevic, "On the probabilistic shaping and geometric shaping in optical communication systems," *IEEE Access*, vol. 7, pp. 21454–21464, 2019.
- [6] K. Ho and J. M. Kahn, "Multilevel optical signals optimized for systems having signal-dependent and signal-independent noises, finite transmitter extinction ratio and intersymbol interference," U.S. Patent 6,690,894, Feb. 10, 2004.
- [7] J. K. Perin, M. Sharif, and J. M. Kahn, "Sensitivity improvement in 100 Gb/s-per-wavelength links using semiconductor optical amplifiers or avalanche photodiodes," *J. Lightw. Technol.*, vol. 34, no. 23, pp. 5542–5553, Dec. 2016.
- [8] G. Katz and E. Sonkin, "Level optimization of PAM-4 transmission with signal-dependent noise," *IEEE Photon. J.*, vol. 11, no. 1, pp. 1–6, Feb. 2019.
- [9] J. Zhang et al., "Experimental demonstration of unequally spaced PAM-4 signal to improve receiver sensitivity for 50-Gbps PON with power-dependent noise distribution," in *Proc. IEEE Opt. Fiber Commun. Conf. Expo.*, 2018, pp. 1–3.
- [10] J. Zhou, L. Gan, Q. Yang, D. Liu, and S. Fu, "Geometric shaping PAM-4 signaling for the simplified coherent receiver with the transmitted signal diversity," in *Proc. Asia Commun. Photon. Conf.*, 2021, pp. 1–3.

- [11] J. Zhou et al., "Unequally spaced PAM-4 signaling enabled sensitivity enhancement of a simplified coherent receiver applied in a UDWDM-PON," *Opt. Exp.*, vol. 30, no. 20, pp. 35369–35380, Sep. 2022. [Online]. Available: <https://opg.optica.org/oe/abstract.cfm?URI=oe-30-20-35369>
- [12] R. van der Linden, N.-C. Tran, E. Tangdiongga, and T. Koonen, "Optimization of flexible non-uniform multilevel PAM for maximizing the aggregated capacity in PON deployments," *J. Lightw. Technol.*, vol. 36, no. 12, pp. 2328–2336, Jun. 2018.
- [13] M. Dalla Santa, C. Antony, G. Talli, and P. D. Townsend, "Power budget improvement in passive optical networks using PAM4 hierarchical modulation," *IEEE Photon. Technol. Lett.*, vol. 29, no. 20, pp. 1747–1750, Oct. 2017.
- [14] B. Karanov et al., "End-to-end deep learning of optical fiber communications," *J. Lightw. Technol.*, vol. 36, no. 20, pp. 4843–4855, Oct. 2018.
- [15] B. Karanov, D. Lavery, P. Bayvel, and L. Schmalen, "End-to-end optimized transmission over dispersive intensity-modulated channels using bidirectional recurrent neural networks," *Opt. Exp.*, vol. 27, no. 14, pp. 19650–19663, Jul. 2019. [Online]. Available: <https://opg.optica.org/oe/abstract.cfm?URI=oe-27-14-19650>
- [16] B. Karanov, L. Schmalen, and A. Alvarado, "Distance-agnostic autoencoders for short reach fiber communications," in *Proc. IEEE Opt. Fiber Commun. Conf. Exhib.*, 2021, pp. 1–3.
- [17] M. P. Yankov, O. Jovanovic, D. Zibar, and F. Da Ros, "Recent advances in constellation optimization for fiber-optic channels," in *Proc. Eur. Conf. Opt. Commun.*, 2022, pp. 1–4.
- [18] S. Yao, A. Mahadevan, Y. Lefevre, N. Kaneda, V. Houtsma, and D. van Veen, "Artificial neural network assisted probabilistic and geometric shaping for flexible rate high-speed PONs," *J. Lightw. Technol.*, vol. 41, no. 16, pp. 5217–5225, Aug. 2023.
- [19] O. Jovanovic, F. Da Ros, D. Zibar, and M. P. Yankov, "Geometric constellation shaping for fiber-optic channels via end-to-end learning," *J. Lightw. Technol.*, vol. 41, no. 12, pp. 3726–3736, Jun. 2023.
- [20] A. V. Oppenheim, J. R. Buck, and R. W. Schafer, *Discrete-Time Signal Processing*, vol. 2. Upper Saddle River, NJ, USA: Prentice Hall, 2001.
- [21] M. Sharif, J. K. Perin, and J. M. Kahn, "Modulation schemes for single-laser 100 Gb/s links: Single-carrier," *J. Lightw. Technol.*, vol. 33, no. 20, pp. 4268–4277, 2015.
- [22] G. P. Agrawal, *Fiber-Optic Communication Systems*, vol. 222, Hoboken, NJ, USA: Wiley, 2012.
- [23] J. Wei, S. Calabró, T. Rahman, and N. Stojanovic, "System aspects of the next-generation data-center networks based on 200G per lambda IMDD links," in *Proc. SPIE*, vol. 11308, pp. 8–15, 2020, doi: [10.1117/12.2542448](https://doi.org/10.1117/12.2542448).
- [24] N. Stojanovic, C. Prodanovic, L. Zhang, and J. Wei, "210/225 Gbit/s PAM-6 transmission with BER below KP4-FEC/EFEC and at least 14 dB link budget," in *Proc. IEEE Eur. Conf. Opt. Commun.*, 2018, pp. 1–3.
- [25] *IEEE Standard for Ethernet - Amendment 10: Media Access Control Parameters, Physical Layers, and Management Parameters for 200 Gb/s and 400 Gb/s Operation*, IEEE Standard 802.3bs-2017, pp. 1–372, Dec. 2017, doi: [10.1109/IEEESTD.2017.8207825](https://doi.org/10.1109/IEEESTD.2017.8207825).
- [26] R. Nagarajan, M. Filer, Y. Fu, M. Kato, T. Rope, and J. Stewart, "Silicon photonics-based 100 Gbit/s, PAM4, DWDM data center interconnects," *J. Opt. Commun. Netw.*, vol. 10, no. 7, pp. 25–36, 2018.
- [27] M. Webster, K. Lakshmikummar, C. Appel, C. Muzio, B. Dama, and K. Shastri, "Low-power MOS-capacitor based silicon photonic modulators and CMOS drivers," in *Proc. IEEE Opt. Fiber Commun. Conf. Exhib.*, 2015, pp. 1–3.
- [28] X. Pang et al., "200 Gbps/lane IM/DD technologies for short reach optical interconnects," *J. Lightw. Technol.*, vol. 38, no. 2, pp. 492–503, 2020.
- [29] A. D. Gallant and J. C. Cartledge, "Characterization of the dynamic absorption of electroabsorption modulators with application to OTDM demultiplexing," *J. Lightw. Technol.*, vol. 26, no. 13, pp. 1835–1839, 2008.
- [30] P. W. Berenguer et al., "Nonlinear digital pre-distortion of transmitter components," *J. Lightw. Technol.*, vol. 34, no. 8, pp. 1739–1745, Apr. 2016.
- [31] C. Eun and E. Powers, "A new volterra predistorter based on the indirect learning architecture," *IEEE Trans. Signal Process.*, vol. 45, no. 1, pp. 223–227, Jan. 1997.
- [32] F. Cappelluti and G. Ghione, "Self-consistent time-domain large-signal model of high-speed traveling-wave electroabsorption modulators," *IEEE Trans. Microw. Theory Techn.*, vol. 51, no. 4, pp. 1096–1104, Apr. 2003.
- [33] G. Ghione, *Semiconductor Devices for High-Speed Optoelectronics*. Cambridge, U.K.: Cambridge Univ. Press, 2009.
- [34] K. Zhang, Q. Zhuge, H. Xin, W. Hu, and D. V. Plant, "Performance comparison of DML, EML and MZM in dispersion-unmanaged short reach transmissions with digital signal processing," *Opt. Exp.*, vol. 26, no. 26, pp. 34288–34304, Dec. 2018. [Online]. Available: <http://opg.optica.org/oe/abstract.cfm?URI=oe-26-26-34288>
- [35] M. Chagnon, "Optical communications for short reach," *J. Lightw. Technol.*, vol. 37, no. 8, pp. 1779–1797, Apr. 2019.
- [36] B. K. Saravanan, "Frequency chirping properties of electroabsorption modulators integrated with laser diodes," Ph.D. dissertation, Universität Ulm, Ulm, Germany, 2006.
- [37] Z. Qu, I. B. Djordjevic, and J. Anderson, "Two-dimensional constellation shaping in fiber-optic communications," *Appl. Sci.*, vol. 9, no. 9, 2019, Art. no. 1889. [Online]. Available: <https://www.mdpi.com/2076-3417/9/9/1889>
- [38] F. Hu, P. Zou, G. Li, W. Yu, and N. Chi, "Enhanced performance of CAP-modulated visible light communication system utilizing geometric shaping and rotation coding," *IEEE Photon. J.*, vol. 11, no. 5, pp. 1–12, Oct. 2019.
- [39] E. Sillekens, G. Liga, D. Lavery, P. Bayvel, and R. I. Killey, "High-cardinality geometrical constellation shaping for the nonlinear fibre channel," *J. Lightw. Technol.*, vol. 40, no. 19, pp. 6374–6387, Oct. 2022.
- [40] B. Chen, C. Okonkwo, H. Hafermann, and A. Alvarado, "Polarization-ring-switching for nonlinearity-tolerant geometrically shaped four-dimensional formats maximizing generalized mutual information," *J. Lightw. Technol.*, vol. 37, no. 14, pp. 3579–3591, Jul. 2019.
- [41] C. Lin, Z. Qu, T. Liu, D. Zou, and I. B. Djordjevic, "Experimental study of capacity approaching general LDPC coded non-uniform shaping modulation format," in *Proc. Asia Commun. Photon. Conf.*, 2016, pp. 1–3.
- [42] S. Zhang et al., "Flex-rate transmission using hybrid probabilistic and geometric shaped 32QAM," in *Proc. Opt. Fiber Commun. Conf. Expo.*, 2018, pp. 1–3.
- [43] S. Zhang, F. Yaman, E. Mateo, T. Inoue, K. Nakamura, and Y. Inada, "A generalized pairwise optimization for designing multi-dimensional modulation formats," in *Proc. IEEE Opt. Fiber Commun. Conf. Exhib.*, 2017, pp. 1–3.
- [44] Z. Qu and I. B. Djordjevic, "Optimal constellation shaping in optical communication systems," in *Proc. IEEE 20th Int. Conf. Transparent Opt. Netw.*, 2018, pp. 1–5.
- [45] T. Liu and I. B. Djordjevic, "Multidimensional optimal signal constellation sets and symbol mappings for block-interleaved coded-modulation enabling ultrahigh-speed optical transport," *IEEE Photon. J.*, vol. 6, no. 4, pp. 1–14, Aug. 2014.
- [46] Z. Qu and I. B. Djordjevic, "Geometrically shaped 16QAM outperforming probabilistically shaped 16QAM," in *Proc. IEEE Eur. Conf. Opt. Commun.*, 2017, pp. 1–3.
- [47] W. Zhou et al., "Adaptive weighted 61-QAM based on geometric shaping in coherent optical communication utilizing k-means algorithm," *Microw. Opt. Technol. Lett.*, vol. 63, no. 9, pp. 2269–2273, 2021.
- [48] S. Zhang and F. Yaman, "Constellation design with geometric and probabilistic shaping," *Opt. Commun.*, vol. 409, pp. 7–12, 2018. [Online]. Available: <https://www.sciencedirect.com/science/article/pii/S0030401817307538>
- [49] A. Mirani, E. Agrell, and M. Karlsson, "Low-complexity geometric shaping," *J. Lightw. Technol.*, vol. 39, no. 2, pp. 363–371, Jan. 2021.
- [50] S. Goossens et al., "Introducing 4D geometric shell shaping for mitigating nonlinear interference noise," *J. Lightw. Technol.*, vol. 41, no. 2, pp. 599–609, Jan. 2023.
- [51] K. Kojima et al., "Nonlinearity-tolerant four-dimensional 2a8PSK family for 5–7 bits/symbol spectral efficiency," *J. Lightw. Technol.*, vol. 35, no. 8, pp. 1383–1391, 2017.
- [52] A. I. Abd El-Rahman and J. C. Cartledge, "Evaluating the impact of QAM constellation subset selection on the achievable information rates of multidimensional formats in fully loaded systems," *J. Lightw. Technol.*, vol. 36, no. 3, pp. 712–720, 2018.
- [53] Z. Qu, S. Zhang, and I. B. Djordjevic, "Universal hybrid probabilistic-geometric shaping based on two-dimensional distribution matchers," in *Proc. Opt. Fiber Commun. Conf. Expo.*, 2018, pp. 1–3.
- [54] J. R. Barry, *Wireless Infrared Communications*, vol. 280. Berlin, Germany: Springer, 1994.
- [55] M. S. Alam et al., "Net 220 Gbps/l IM/DD transmission in O-band and C-band with silicon photonic traveling-wave MZM," *J. Lightw. Technol.*, vol. 39, no. 13, pp. 4270–4278, Jul. 2021.

- [56] R. Nagarajan and I. Lyubomirsky, "Next-gen data center interconnects: The race to 800G," *COBO Webcast*, 2021. Accessed: Oct. 19, 2023. [Online]. Available: https://www.onboardoptics.org/_files/ugd/8abefc_c515c73a6fca4ea1809b6981674fdf1f.pdf
- [57] J. Johnson, "Chirp characteristics and chromatic dispersion tolerance of 200G EML transmitters," IEEE P802.3df Oct. 2022 Session, 2022.
- [58] *IEEE standard for ethernet amendment 9: Physical layer specifications and management parameters for 25 Gb/s and 50 Gb/s passive optical networks*, IEEE Std 802.3ca-2020, 2020.
- [59] T. Wettlin, S. Calabró, T. Rahman, J. Wei, N. Stojanovic, and S. Pachnicke, "DSP for high-speed short-reach IM/DD systems using PAM," *J. Lightw. Technol.*, vol. 38, no. 24, pp. 6771–6778, Dec. 2020.
- [60] N. Stojanovic, F. Karinou, Z. Qiang, and C. Prodaniuc, "Volterra and wiener equalizers for short-reach 100G PAM-4 applications," *J. Lightw. Technol.*, vol. 35, no. 21, pp. 4583–4594, 2017.
- [61] Y. Yu, M. R. Choi, T. Bo, Z. He, Y. Che, and H. Kim, "Low-complexity second-order volterra equalizer for DML-based IM/DD transmission system," *J. Lightw. Technol.*, vol. 38, no. 7, pp. 1735–1746, 2020.
- [62] C. Schmidt et al., "Data converter interleaving: Current trends and future perspectives," *IEEE Commun. Mag.*, vol. 58, no. 5, pp. 19–25, May 2020.
- [63] P. Runge et al., "InP-components for 100 GBaud optical data center communication," *Photonics*, vol. 8, no. 1, 2021, Art. no. 18. [Online]. Available: <https://www.mdpi.com/2304-6732/8/1/18>
- [64] P. Torres-Ferrera, V. Ferrero, M. Valvo, and R. Gaudino, "Impact of the overall electrical filter shaping in next-generation 25 and 50 Gb/s PONs," *J. Opt. Commun. Netw.*, vol. 10, no. 5, pp. 493–505, 2018.
- [65] S. Hranilovic, "Minimum-bandwidth optical intensity Nyquist pulses," *IEEE Trans. Commun.*, vol. 55, no. 3, pp. 574–583, Mar. 2007.
- [66] C. B. Czegledi, M. R. Khanzadi, and E. Agrell, "Bandlimited power-efficient signaling and pulse design for intensity modulation," *IEEE Trans. Commun.*, vol. 62, no. 9, pp. 3274–3284, Sep. 2014.
- [67] M. Mazzini et al., "25GBaud PAM-4 error free transmission over both single mode fiber and multimode fiber in a QSFP form factor based on silicon photonics," in *Proc. IEEE Opt. Fiber Commun. Conf. Exhib.*, 2015, pp. 1–3.
- [68] C. Chen, X. Tang, and Z. Zhang, "Transmission of 56-Gb/s PAM-4 over 26-km single mode fiber using maximum likelihood sequence estimation," in *Proc. Opt. Fiber Commun. Conf. Exhib.*, 2015, pp. 1–3.
- [69] P. Gou, L. Zhao, K. Wang, W. Zhou, and J. Yu, "Nonlinear look-up table predistortion and chromatic dispersion precompensation for IM/DD PAM-4 transmission," *IEEE Photon. J.*, vol. 9, no. 5, pp. 1–7, Oct. 2017.
- [70] J. Zhang, J. Yu, and H.-C. Chien, "EML-based IM/DD 400G (4×112.5 -Gbit/s) PAM-4 over 80km SSMF based on linear pre-equalization and nonlinear LUT pre-distortion for inter-DCI applications," in *Proc. Opt. Fiber Commun. Conf. Exhib.*, 2017, pp. 1–3.
- [71] H. Li et al., "A 3-D-integrated silicon photonic microring-based 112-Gb/s PAM-4 transmitter with nonlinear equalization and thermal control," *IEEE J. Solid-State Circuits*, vol. 56, no. 1, pp. 19–29, Jan. 2021.
- [72] B. Milivojevic, S. Wiese, S. Anderson, T. Brenner, M. Webster, and B. Dama, "Demonstration of optical transmission at bit rates of up to 321.4 Gb/s using compact silicon based modulator and linear BiCMOS MZM driver," *J. Lightw. Technol.*, vol. 35, no. 4, pp. 768–774, 2017.
- [73] A. Samani et al., "Silicon photonic Mach-Zehnder modulator architectures for on chip PAM-4 signal generation," *J. Lightw. Technol.*, vol. 37, no. 13, pp. 2989–2999, Jul. 2019.